

International Journal of Geomechanics

Finite strains effects in 3D fully coupled geomechanical simulations

--Manuscript Draft--

Manuscript Number:	GMENG-3287R1	
Full Title:	Finite strains effects in 3D fully coupled geomechanical simulations	
Manuscript Region of Origin:	ITALY	
Article Type:	Technical Paper	
Manuscript Classifications:	1.1: Finite Element Methods; 2.1: Soils: Clays and Sands; 4.6: Seepage & Groundwater Flow	
Funding Information:	Italian Ministry of Education, University and Research (MIUR) (Project PRIN "COAN 5.50.16.01" - code 2015JW9NJT)	Not applicable
Abstract:	<p>Numerical modelling of geomechanical phenomena and geo-engineering problems often involves complex issues related to several variables and corresponding coupling effects. Under certain circumstances, both soil and rock may experience a non-linear material response, due to e.g. plastic, viscous or damage behavior, and even a non-linear geometric one, due to large deformations/displacements of the solid. Furthermore, the presence of one or more fluids (water, oil, gas, etc.) within the skeleton must be accounted for when evaluating the interaction between the different phases of the continuum body.</p> <p>A multiphase three-dimensional coupled model in finite strains, suitable for dealing with solid-displacements/fluid-diffusion problems, is here described and an elasto-plastic behavior for the solid phase is assumed.</p> <p>Particularly, a 3D mixed finite element is implemented to fulfill stability requirements of the adopted formulation, as well as a permeability tensor dependent on deformation is introduced.</p> <p>A consolidation scenario induced by filling of silos is investigated and the effects of the adoption of finite strains discussed.</p>	
Corresponding Author:	Nico De Marchi, M.E. Universita degli Studi di Padova Padova, Padova ITALY	
Corresponding Author E-Mail:	nico.demarchi@dicea.unipd.it	
Order of Authors:	Nico De Marchi, M.E. Valentina A. Salomoni, Prof. Nicolò Spiezia, Ph.D.	
Suggested Reviewers:	<p>Kaspar Willam, Prof. University of Colorado Boulder willam@colorado.edu Expert in the field of non-linear modelling of porous media</p> <p>Francesco Marotti de Sciarra, Prof. Universita degli Studi di Napoli Federico II francesco.marottidesciarra@unina.it Expert in the field of non-linear modelling of porous media</p> <p>Angelo Marcello Tarantino, Prof. Universita degli Studi di Modena e Reggio Emilia angelomarcello.tarantino@unimore.it Expert in the field of non-linear modelling of porous media</p>	
Opposed Reviewers:		
Additional Information:		
Question	Response	

<p>Authors are required to attain permission to re-use content, figures, tables, charts, maps, and photographs for which the authors do not hold copyright. Figures created by the authors but previously published under copyright elsewhere may require permission. For more information see http://ascelibrary.org/doi/abs/10.1061/9780784479018.ch03. All permissions must be uploaded as a permission file in PDF format. Are there any required permissions that have not yet been secured? If yes, please explain in the comment box.</p>	<p>No</p>
<p>ASCE does not review manuscripts that are being considered elsewhere to include other ASCE Journals and all conference proceedings. Is the article or parts of it being considered for any other publication? If your answer is yes, please explain in the comments box below.</p>	<p>No</p>
<p>Is this article or parts of it already published in print or online in any language? ASCE does not review content already published (see next questions for conference papers and posted theses/dissertations). If your answer is yes, please explain in the comments box below.</p>	<p>No</p>
<p>Has this paper or parts of it been published as a conference proceeding? A conference proceeding may be reviewed for publication only if it has been significantly revised and contains 50% new content. Any content overlap should be reworded and/or properly referenced. If your answer is yes, please explain in the comments box below and be prepared to provide the conference paper.</p>	<p>No</p>
<p>ASCE allows submissions of papers that are based on theses and dissertations so long as the paper has been modified to fit the journal page limits, format, and tailored for the audience. ASCE will consider such papers even if the thesis or dissertation has been posted online provided that the degree-granting institution requires that the thesis or dissertation be posted.</p> <p>Is this paper a derivative of a thesis or dissertation posted or about to be posted on the Internet? If yes, please provide the URL or DOI permalink in the comment box below.</p>	<p>No</p>

<p>Each submission to ASCE must stand on its own and represent significant new information, which may include disproving the work of others. While it is acceptable to build upon one's own work or replicate other's work, it is not appropriate to fragment the research to maximize the number of manuscripts or to submit papers that represent very small incremental changes. ASCE may use tools such as CrossCheck, Duplicate Submission Checks, and Google Scholar to verify that submissions are novel. Does the manuscript constitute incremental work (i.e. restating raw data, models, or conclusions from a previously published study)?</p>	<p>No</p>
<p>Authors are expected to present their papers within the page limitations described in Publishing in ASCE Journals: A Guide for Authors. Technical papers and Case Studies must not exceed 30 double-spaced manuscript pages, including all figures and tables. Technical notes must not exceed 7 double-spaced manuscript pages. Papers that exceed the limits must be justified. Grossly over-length papers may be returned without review. Does this paper exceed the ASCE length limitations? If yes, please provide justification in the comments box below.</p>	<p>No</p>
<p>All authors listed on the manuscript must have contributed to the study and must approve the current version of the manuscript. Are there any authors on the paper that do not meet these criteria? If the answer is yes, please explain in the comments.</p>	<p>No</p>
<p>Was this paper previously declined or withdrawn from this or another ASCE journal? If so, please provide the previous manuscript number and explain what you have changed in this current version in the comments box below. You may upload a separate response to reviewers if your comments are extensive.</p>	<p>Yes</p>
<p>Please provide the previous manuscript number and explain what you have changed in this current version in the comments box below. You may upload a separate response to reviewers if your comments are extensive.</p> <p>as follow-up to "Was this paper previously declined or withdrawn from this or another ASCE journal? If so, please</p>	<p>Please consider that the previous manuscript GTENG-6840 was examined by the Chief Editor Prof. Mohammed (ASCE Journal of Geotechnical and Geoenvironmental Engineering) who suggested us to submit it to IJOG because "the scope is a better match for our companion journal IJOG (...) I believe the innovation and scope best fit/serve the journal" (i.e. IJOG). The manuscript has been examined by the Editor only, it has NOT been reviewed</p>

<p>provide the previous manuscript number and explain what you have changed in this current version in the comments box below. You may upload a separate response to reviewers if your comments are extensive.</p> <p>"</p>	
<p>Companion manuscripts are discouraged as all papers published must be able to stand on their own. Justification must be provided to the editor if an author feels as though the work must be presented in two parts and published simultaneously. There is no guarantee that companions will be reviewed by the same reviewers, which complicates the review process, increases the risk for rejection and potentially lengthens the review time. If this is a companion paper, please indicate the part number and provide the title, authors and manuscript number (if available) for the companion papers along with your detailed justification for the editor in the comments box below. If there is no justification provided, or if there is insufficient justification, the papers will be returned without review.</p>	
<p>If this manuscript is intended as part of a Special Issue or Collection, please provide the Special Collection title and name of the guest editor in the comments box below.</p>	
<p>Recognizing that science and engineering are best served when data are made available during the review and discussion of manuscripts and journal articles, and to allow others to replicate and build on work published in ASCE journals, all reasonable requests by reviewers for materials, data, and associated protocols must be fulfilled. If you are restricted from sharing your data and materials, please explain below.</p>	
<p>Papers published in ASCE Journals must make a contribution to the core body of knowledge and to the advancement of the field. Authors must consider how their new knowledge and/or innovations add value to the state of the art and/or state of the practice. Please outline the specific contributions of this research in the comments box.</p>	<p>Within the research field of non-linear modelling of porous media, the paper contributes to underline the consequences of accounting for finite strains when studying soil-structure interactions in consolidation scenarios. Particularly, it is evidenced that for realistically reconstructing the hazard of silos rotation and tilting, a non-linear geometric approach must be followed. The model is improved by a dependence of the permeability tensor from deformation, as well as by the introduction of an enriched Finite Element able to fulfill stability requirements of the adopted approach.</p>
<p>The flat fee for including color figures in print is \$800, regardless of the number of color figures. There is no fee for online only color figures. If you decide to not print figures in color, please ensure that</p>	<p>No</p>

<p>the color figures will also make sense when printed in black-and-white, and remove any reference to color in the text. Only one file is accepted for each figure. Do you intend to pay to include color figures in print? If yes, please indicate which figures in the comments box.</p>	
<p>If there is anything else you wish to communicate to the editor of the journal, please do so in this box.</p>	

Finite strains effects in 3D fully coupled geomechanical simulations

Nico De Marchi¹, Valentina Salomoni², and Nicolò Spiezia³

¹Dr., Dept. of Civil, Environmental and Architectural Engineering, University of Padua, via Marzolo 9, 35121 Padua, Italy. E-mail: nico.demarchi@dicea.unipd.it

²Prof., Dept. of Management and Engineering, University of Padua, via Stradella S. Nicola 3, 36100 Vicenza, Italy. E-mail: valentina.salomoni@unipd.it

³Dr., Dept. of Civil, Environmental and Architectural Engineering, University of Padua, via Marzolo 9, 35121 Padua, Italy. E-mail: nicolo.spiezia@dicea.unipd.it

ABSTRACT

Numerical modelling of geomechanical phenomena and geo-engineering problems often involves complex issues related to several variables and corresponding coupling effects. Under certain circumstances, both soil and rock may experience a non-linear material response, due to e.g. plastic, viscous or damage behavior, and even a non-linear geometric one, due to large deformations/displacements of the solid. Furthermore, the presence of one or more fluids (water, oil, gas, etc.) within the skeleton must be accounted for when evaluating the interaction between the different phases of the continuum body. A multiphase three-dimensional coupled model in finite strains, suitable for dealing with solid-displacements/fluid-diffusion problems, is here described and an elasto-plastic behavior for the solid phase is assumed. Particularly, a 3D mixed finite element is implemented to fulfill stability requirements of the adopted formulation, as well as a permeability tensor dependent on deformation is introduced. A consolidation scenario induced by filling of silos is investigated and the effects of the adoption of finite strains discussed.

Keywords: Porous media, multiphase problems, finite strains, elasto-plasticity, Finite Element Method.

INTRODUCTION

Geomaterials such as soil, rock or concrete, are basic materials in the civil engineering field, with many different applications. The description of their mechanical behavior is a challenging task, requiring sophisticated numerical analyses. Particularly, such materials must be considered as multiphase porous media, composed by a solid skeleton and one (or even more) fluid within the pores. Hence, geomechanical problems are characterized by solid-fluid interaction, due to the presence of overlapping phases, and correspondingly a coupled analysis is required (Lewis and Schrefler 1998). Further, geomaterials can also experience material non-linearities of the solid skeleton, e.g. due to plasticity, creep or damage. Even in the elastic regime, the mechanical behavior of geomaterials is often non-linear.

Depending on the phenomenon to model, it may be necessary to take into account finite deformations, so introducing a source of geometric non-linearity in the formulation of the problem (Wang et al. 2009). Examples of geomechanical problems where finite deformations are involved are the inception of slopes (Lee et al. 2012; Zhu and Randolph 2009; Mohammadi and Taiebat 2014), the consolidation of heavy structures over soft soils (Bienen et al. 2015; Andresen et al. 2010), the excavation of tunnels (Meguid et al. 2002) and wellbores (Spiezia et al. 2016), the consolidation settlements around pile foundations (Osman and Randolph 2011; Zhang et al. 2015) and the consolidation of mine waste tailings (Caldwell et al. 1984), just to recall a few.

In the last two decades, theoretical and computational research has provided wide support for the solution of this kind of problems, where large deformations are encountered. Although several innovative methods have been proposed in literature, such as the Smoothed Particle Hydrodynamics (SPH) (Wang et al. 2016), the Material Point Method (MPM) (Abe et al. 2013), the Particle Finite Element Method (PFEM) (Carbonell et al. 2009) and the Meshless Local Petrov-Galerkin (MLPG) (Atluri and Zhu 1998), the Finite Element Method (FEM) is still probably the most widely used tool. It allows to solve the set of differential equations arising from the imposition of the balance equations to a continuum multiphase body, computing displacements, stress and strain fields, pressures etc. for the solid-fluid mixture. By using a FEM approach (Hughes 2012; Wriggers 2008),

52 finite strains can be rigorously taken into account as an extension of the infinitesimal framework,
53 adopting an adequate formulation for both the balance laws and the constitutive model.

54 Even though the theory for coupled poromechanics in finite strains, solved within the framework of
55 FEM, has been proposed in the late nineties by the pioneer works of Simo et al. (Simo and Meschke
56 1993), Borja et al. (Borja and Alarcón 1995; Borja et al. 1998) and Armero et al. (Armero 1999),
57 this subject presents still some aspects that are worth being studied further.

58 In fact, even if in some recent works the effects of assuming finite strains when simulating geotech-
59 nical problems have been investigated (Nazem et al. 2006; Kardani et al. 2013; Zhang et al. 2018),
60 only a few take into account the coupling between the different phases (Huang et al. 2014; Singh
61 et al. 2016; Qi et al. 2017), which is an aspect of relevance when dealing with porous materials.

62 Hence in this work a coupled hygro–mechanical model in finite strains (Borja 2013) based on the
63 modified mixture theory (Borja et al. 1998) is presented, following the lines of (Spiezia et al. 2016)
64 for saturated porous media.

65 Particularly, the approach takes advantage of a constitutive model (Borja and Tamagnini 1998)
66 which has demonstrated to be particularly suitable in predicting different features of the granular
67 materials as pressure sensitivity, hardening response with large plastic volumetric compaction,
68 softening response with plastic dilation and coupled volumetric deviatoric plastic deformations.
69 The model has been upgraded via the introduction of a permeability tensor variable with the de-
70 formation of the solid skeleton, as well as of a specific type of hexahedral elements, developed to
71 guarantee solvability and stability of mixed formulations (Brezzi and Bathe 1990). The paper is
72 organized as follows.

73 First, the balance equations, together with the constitutive laws for both the fluid and the solid
74 phase, are briefly recalled (Borja and Alarcón 1995; Borja et al. 1998; Song and Borja 2014).

75 Section 2 presents the numerical implementation of the developed equations, describing in detail
76 the formulation of the three-dimensional code and its novel features.

77 Section 3 presents the validation of the code, by comparing the results with the benchmark cases
78 described in (Borja et al. 1998) and with the experimental results reported in (Callari et al. 1998;

79 [Al-Tabbaa 1987](#)).

80 Section 4 presents the numerical simulation of a consolidation process due to the filling of two
81 tall structures over a fully saturated domain, evidencing the code capabilities in simulating soil–
82 structure interaction.

83 Notations and symbols used throughout the paper are as follows: bold-face letters denote matrices
84 and vectors; the symbol ‘ \cdot ’ denotes an inner product of two vectors (e.g. $\mathbf{a} \cdot \mathbf{b} = a_i b_i$) or a single
85 contraction of adjacent indices of two tensors (e.g. $\mathbf{c} \cdot \mathbf{d} = c_{ij} d_{jk}$); the symbol ‘ $:$ ’ denotes an
86 inner product of two second-order tensors (e.g. $\mathbf{c} : \mathbf{d} = c_{ij} d_{ij}$), or a double contraction of adjacent
87 indices of tensor of rank two and higher (e.g. $\mathbf{C} : \boldsymbol{\epsilon}^e = C_{ijkl} \epsilon_{kl}^e$); the symbol ‘ \otimes ’ denotes a
88 juxtaposition, e.g. $(\mathbf{a} \otimes \mathbf{b})_{ij} = a_i b_j$. For any symmetric second-order tensor $\boldsymbol{\alpha}$ and $\boldsymbol{\beta}$ we have
89 $(\boldsymbol{\alpha} \otimes \boldsymbol{\beta})_{ijkl} = \alpha_{ij} \beta_{kl}$, $(\boldsymbol{\alpha} \ominus \boldsymbol{\beta})_{ijkl} = \alpha_{il} \beta_{jk}$ and $(\boldsymbol{\alpha} \oplus \boldsymbol{\beta})_{ijkl} = \alpha_{jl} \beta_{ik}$. A positive stress is also
90 assumed for tension according to the solid mechanics convention.

91 THEORETICAL FRAMEWORK

92 This section briefly recalls the coupled balance laws for a fully saturated porous media ([Borja](#)
93 [and Alarcón 1995](#)), together with the constitutive model for both solid and fluid phase.

94 Balance laws

95 In agreement with the mixture theory and by assuming incompressibility of the two phases, the
96 balance of linear momentum and the balance of mass for a fully saturated porous medium in the
97 quasi static regime are

$$\rho \mathbf{g} + \operatorname{div} \tilde{\boldsymbol{\sigma}} = 0; \quad (1)$$

$$\operatorname{div} \mathbf{v} + \operatorname{div} [\varphi(\mathbf{v}^F - \mathbf{v})] = 0, \quad (2)$$

98 where $\rho_0 = J\rho$ is the reference mass density, \mathbf{g} the vector of gravity acceleration, $\tilde{\boldsymbol{\sigma}}$ the total Cauchy
99 stress tensor, related to the total Kirchhoff stress tensor $\tilde{\boldsymbol{\tau}}$ and the total first Piola-Kirchhoff tensor

100 $\tilde{\mathbf{P}}$ (Marsden and Hughes 1994) via the following expression

$$101 \quad \tilde{\mathbf{P}} = \tilde{\boldsymbol{\tau}} \cdot \mathbf{F}^{-T} = J \tilde{\boldsymbol{\sigma}} \cdot \mathbf{F}^{-T}. \quad (3)$$

102 The term J is the Jacobian defined from the deformation gradient \mathbf{F} of the motion ϕ

$$103 \quad J = \det(\mathbf{F}); \quad \mathbf{F} = \frac{\partial \phi}{\partial \mathbf{X}}; \quad \phi = \mathbf{X} + \mathbf{u}. \quad (4)$$

104 In Eq. (2), \mathbf{v} is the vector the solid phase velocity vector, \mathbf{v}^F is the fluid phase intrinsic velocity and
 105 φ is the porosity of the soil skeleton defined through the Jabacobian as

$$106 \quad \varphi = \frac{JdV - (1 - \varphi_0)dV}{JdV} = 1 - \frac{(1 - \varphi_0)}{J}. \quad (5)$$

107 The term $\varphi(\mathbf{v}^F - \mathbf{v})$ represents the Darcy velocity $\tilde{\mathbf{v}}$, defined as the relative volumetric rate of fluid
 108 per unit area through the deforming soil mass.

109 Constitutive models

110 Solid phase

111 For the description of the elasto-plastic mechanical behavior of the solid we employ the multi-
 112 plicative decomposition of the deformation gradient and the product formula algorithm described
 113 by Simo (Simo 1992)

$$114 \quad \mathbf{F} = \frac{\partial \phi}{\partial \mathbf{x}^u} \cdot \frac{\partial \mathbf{x}^u}{\partial \mathbf{X}} \equiv \mathbf{F}^e \cdot \mathbf{F}^p; \quad \forall \mathbf{X} \in \mathcal{B}; \quad t \geq 0, \quad (6)$$

115 where \mathbf{x}^u is the intermediate unloaded configuration. From the second law of thermodynamics we
 116 can define the following set of constitutive relations describing the elastoplastic process

$$117 \quad \boldsymbol{\tau} = 2 \frac{\partial \Psi}{\partial \mathbf{b}^e} \cdot \mathbf{b}^e; \quad -\frac{1}{2} \mathcal{L}_v \mathbf{b}^e = \dot{\gamma} \frac{\partial \mathcal{F}}{\partial \boldsymbol{\tau}} \cdot \mathbf{b}^e; \quad \dot{\xi} = \dot{\gamma} \frac{\partial \mathcal{F}}{\partial \boldsymbol{\chi}}, \quad (7)$$

118 where $\Psi = \Psi(X, \mathbf{b}^e, \xi)$ is the stored energy function, $\mathbf{b}^e = \mathbf{F}^e \cdot \mathbf{F}^{eT}$ the left elastic Cauchy-Green
 119 strain tensor, ξ a plastic variable and $\chi = \partial\Psi/\partial\xi$ the hardening response of the solid matrix. The
 120 quantity $\mathcal{L}_\gamma \mathbf{b}^e$ is the Lie derivative of \mathbf{b}^e , while \mathcal{F} is the yield function and $\dot{\gamma}$ is a non-negative
 121 plastic multiplier satisfying the Kuhn-Tucker conditions: $\dot{\gamma} \geq 0$, $\mathcal{F}(\boldsymbol{\tau}, \chi) \leq 0$ and $\dot{\gamma}\mathcal{F}(\boldsymbol{\tau}, \chi) = 0$.

122 The elastic left Cauchy-Green tensor \mathbf{b}^e and the Kirchhoff effective stress tensor $\boldsymbol{\tau}$ can be
 123 expressed through the spectral decomposition

$$124 \quad \mathbf{b}^e = \sum_{A=1}^3 (\lambda_A^e)^2 \mathbf{m}^{(A)}; \quad \boldsymbol{\tau} = \sum_{A=1}^3 \boldsymbol{\beta}_A \mathbf{m}^{(A)}, \quad \mathbf{m}^{(A)} = \mathbf{n}^{(A)} \otimes \mathbf{n}^{(A)}, \quad (8)$$

125 where λ_A^e are the the elastic principal stretches, $\boldsymbol{\beta}_A$ the principal Kirchhoff effective stresses and
 126 $\mathbf{n}^{(A)}$ the principal direction for both strains and stresses thanks to isotropy assumption. Together
 127 with frame indifference assumption, the free energy can be written as a function of the elastic
 128 principal strains

$$129 \quad \Psi(X, \mathbf{b}^e) = \Psi(X, \varepsilon_1^e, \varepsilon_2^e, \varepsilon_3^e); \quad \varepsilon_A^e = \ln(\lambda_A^e); \quad A = 1, 2, 3, \quad (9)$$

130 where ε_A^e are the principal elastic logarithmic strains, and from the first relation of Eq. (7) we obtain
 131 the following relation

$$132 \quad \boldsymbol{\beta}_A = \frac{\partial\Psi}{\partial\varepsilon_A^e}; \quad A = 1, 2, 3. \quad (10)$$

133 In the present work, we adopt the following stored energy function (Borja and Tamagnini 1998)
 134 describing the elastic response of the soil in terms of volumetric ε_v^e and deviatoric ε_s^e elastic strain
 135 invariants

$$136 \quad \Psi(\varepsilon_v^e, \varepsilon_s^e) = \tilde{\Psi}(\varepsilon_v^e) + \frac{3}{2} \mu^e \varepsilon_s^{e2}, \quad (11)$$

$$137 \quad \tilde{\Psi}(\varepsilon_v^e) = -P_0 \hat{k} \exp \Omega; \quad \Omega = -\frac{\varepsilon_v^e - \varepsilon_{v0}^e}{\hat{k}}; \quad \mu^e = \mu_0 + \frac{\alpha}{\hat{k}} \tilde{\Psi}, \quad (12)$$

139 where $\tilde{\Psi}$ is the contribution given by the isotropic part, \hat{k} the elastic compressibility index, μ^e the
 140 elastic shear modulus, μ_0 a constant term, α a parameter coupling shear and volumetric parts and

141 finally P_0 the mean reference normal Kirchhoff stress invariant. The yield function is given by

$$142 \quad \tilde{\mathcal{F}}(P, Q, P_c) = \frac{Q^2}{M^2} + P(P - P_c) = 0, \quad (13)$$

143 where P and Q are the effective Kirchhoff stress invariants, P_c the Kirchhoff preconsolidation
144 pressure defining the size of the ellipsoid and M the slope of the critical state line, as shown in
145 Fig. 1.

146 The model assumes a bi-logarithmic hardening law, as shown in Fig. 2, described by the
147 following equation

$$148 \quad \ln\left(\frac{v}{v_0}\right) = -\hat{\lambda} \ln\left(\frac{P_c}{P_{c0}}\right), \quad (14)$$

149 where $\hat{\lambda}$ is the virgin compression index, $v = V/V_S = 1 + e$ the specific volume of the soil and v_0 a
150 reference value.

151 The hardening law governing the expansion/contraction of the ellipse through the parameter P_c is
152 given by

$$153 \quad \frac{\dot{P}_c}{P_c} = -\Theta \dot{\varepsilon}_v^p, \quad (15)$$

154 with $\Theta = 1/(\hat{\lambda} - \hat{\kappa})$.

155 *Fluid phase*

156 For the fluid phase, assuming laminar flow, the model adopts the generalized Darcy's law

$$157 \quad \tilde{\mathbf{v}} = -\mathbf{k} \cdot \text{grad } \Pi, \quad (16)$$

158 where $\tilde{\mathbf{v}} = \varphi(\mathbf{v}^F - \mathbf{v})$ is the Darcy velocity and Π is the total fluid potential defined as

$$159 \quad \Pi = \Pi^p + \Pi^e = \frac{p}{g \rho_F} - \Pi^e, \quad (17)$$

160 where Π^p is the pressure potential with p the the Cauchy pore pressure and ρ_F the mass density
161 of the fluid; Π^e is the elevation potential. Finally, \mathbf{k} is the second order permeability tensor,

162 which is assumed to be dependent on the deformation of the solid skeleton through the Jacobian J ,
 163 introducing therefore an additional source of non-linearity with respect to the original formulation
 164 proposed in (Borja et al. 1998).

165 According to the Kozeny-Carman equation (Song and Borja 2014), the permeability reads

$$166 \quad k(J) = \frac{\rho_F g}{\mu} \frac{D^2}{180} \frac{[J - (1 - \varphi_0)]^3}{J(1 - \varphi_0)^2} \mathbf{1}, \quad (18)$$

167 where D is the effective diameter of the grains, μ the dynamic viscosity of water, φ_0 the initial
 168 porosity of the solid and $\mathbf{1}$ the second order identity tensor.

169 NUMERICAL IMPLEMENTATION

170 Variational equations

171 For developing the variational counterpart of Eqs. (1) and (2), following the approach proposed
 172 in (Borja and Alarcón 1995), we consider a fully saturated solid domain $\mathcal{B} \in R^{n_{sd}}$ and define the
 173 motion of the solid phase ϕ , its first variation η , the Cauchy pore pressure p and its first variation
 174 ψ . The variational equation of the linear momentum G reads

$$175 \quad G(\phi, p, \eta) = \int_{\mathcal{B}} (\text{grad } \eta : \tilde{\tau} - \rho_0 \eta \cdot \mathbf{g}) dV - \int_{\partial \mathcal{B}^e} \eta \cdot \mathbf{t} dA = 0, \quad (19)$$

176 and the variational equation of the mass balance equation H reads

$$177 \quad H(\phi, p, \psi) = \int_{\phi_t(\mathcal{B})} (\psi \text{div } \mathbf{v} - \text{grad } \psi \cdot \tilde{\mathbf{v}}) dv - \int_{\partial \phi_t^h(\mathcal{B})} \psi q da = 0. \quad (20)$$

178 These field equations G and H are expressed in the Eulerian form for developing an *updated*
 179 *Lagrangian* formulation, allowing for obtaining the solution of the non-linear coupled problem.
 180 We rewrite the equations in the following way

$$181 \quad G(\phi, p, \eta) = \int_{\mathcal{B}} (\text{grad } \eta : \tau - Jp \text{div } \eta - J\rho \eta \cdot \mathbf{g}) dV - \int_{\partial \mathcal{B}^e} \eta \cdot \mathbf{t} dA; \quad (21)$$

$$H(\phi, p, \psi) = \int_{\mathcal{B}} \psi \dot{J} dV + \int_{\mathcal{B}} \text{grad } \psi \cdot \frac{J\mathbf{k}}{g\rho_F} \cdot (\text{grad } p - \rho_F \mathbf{g}) dV - \int_{\partial\mathcal{B}^h} \psi Q dA. \quad (22)$$

In the first equation, the total Kirchhoff stress tensor has been decomposed into the effective part $\boldsymbol{\tau}$ and the pore pressure part Jp , through the classical Terzaghi's formula. The second equation is obtained from the definition of the Darcy's velocity, recalling that the time derivative of the Jacobian J is equal to $\dot{J} = J \text{div } \mathbf{v}$ (Marsden and Hughes 1994). Furthermore this integral is formulated with respect to the initial configuration \mathcal{B} , and hence $d\mathbf{v} = JdV$ has been substituted. \mathbf{t} is the prescribed stress vector on the boundary $\partial\mathcal{B}^t$ and Q is the prescribed rate of flux across the boundary $\partial\mathcal{B}^h$, assumed as positive when the fluid goes into the solid matrix. The condition $q = Q = 0$ means that no fluid flows through the boundary. The presence of \dot{J} inside Eq. (22) requires the semi-discretization of the second variational equation

$$\begin{aligned} H_{\Delta t}(\phi, \theta, \psi) = & \int_{\mathcal{B}} \frac{\psi}{\Delta t} (J_{n+1} - J_n) dV \\ & - \int_{\mathcal{B}} [\beta (\text{grad } \psi \cdot J\tilde{\mathbf{v}})_{n+1} + (1 - \beta) (\text{grad } \psi \cdot J\tilde{\mathbf{v}})_n] dV \\ & \int_{\partial\mathcal{B}} \psi [\beta Q_{n+1} + (1 - \beta) Q_n] dA, \end{aligned} \quad (23)$$

where $\Delta t = t_{n+1} - t_n$ and β is the trapezoidal integration parameter defining the three time integration schemes: for $\beta = 0$ the Explicit Euler, for $\beta = 1/2$ the Crank-Nicolson and for $\beta = 1$ the Implicit Euler scheme, respectively.

The first variation of the variational equations $G(\phi, \theta, \boldsymbol{\eta})$ and $H(\phi, \theta, \psi)$, necessary for the solution of the problem through a Newton-Raphson scheme, is reported in Appendix A. By comparing the equations with those proposed in (Borja et al. 1998), a new contribution arises (see Eq. (45)), due to the permeability variation of the porous medium. The variation of the second order permeability tensor \mathbf{k} with respect to the Jacobian of the gradient tensor J gives

$$\mathbf{k}'(J) = \frac{\partial \mathbf{k}}{\partial J} = \frac{\rho_F g}{\mu} \frac{D^2}{180} \frac{3[J - (1 - \varphi_0)]^2 J - [J - (1 - \varphi_0)]^3}{J^2(1 - \varphi_0)^2} \mathbf{1}. \quad (24)$$

Numerical integration

A three-dimensional mixed finite element has been implemented within the research code, which combines a three-quadratic 20–node displacement interpolation with a three-linear 8–node pore pressure interpolation (Fig. 3), so to fulfill the necessary stability requirements, satisfy the ellipticity requirement and the Ladyzhenskaya-Babuška-Brezzi (LBB) condition (Brezzi and Bathe 1990; Arnold 1990). The adopted element belongs to the Taylor-Hood family (Arnold et al. 1984; Guzmán and Sánchez 2015), in which the displacement interpolation is one-order higher than the pressure one. By assuming a quadratic order function for the displacement field, the continuity for the stress/strain field is also guaranteed.

Correspondingly, $N^\phi(\mathbf{x})$ and $N^p(\mathbf{x})$ indicate the shape function for the solid phase ϕ and the pore pressure field p . The displacements field $\mathbf{u}^h(\mathbf{x}) \in R^{n_{sd}}$, with $n_{sd} = 3$ becomes

$$\mathbf{u}^h(\mathbf{x}) = N^\phi(\mathbf{x})\{\mathbf{d} + \mathbf{d}_g\}, \quad (25)$$

where $\mathbf{d} \in R^{NQ}$ and \mathbf{d}_g are the unknown nodal displacements and the prescribed nodal displacements vector, respectively, $NQ=20$. In the same way, the pore pressure field $p^h(\mathbf{x}) \in R^1$ is expressed as

$$p^h(\mathbf{x}) = N^p(\mathbf{x})\{\mathbf{p} + p_r\}, \quad (26)$$

where $\mathbf{p} \in R^{NP}$ is the unknown nodal pore pressures vector while p_r is the prescribed nodal pore pressures vector, with $NP=8$. The weight functions η and ψ may be written as

$$\eta^h(\mathbf{x}) = N^\phi(\mathbf{x})\tilde{\eta}; \quad \psi^h(\mathbf{x}) = N^p(\mathbf{x})\tilde{\psi}, \quad (27)$$

where $\tilde{\eta} \in R^{NQ}$ and $\tilde{\psi} \in R^{NP}$. The discretized form of Eq. (21) becomes

$$G^h(\phi, p, \tilde{\eta}) = \tilde{\eta}^T [N^S(\mathbf{d}) + N^F(\mathbf{p}) - \mathbf{F}_{EXT}] = \mathbf{0}, \quad (28)$$

222 where:

$$\mathbf{N}^S(\mathbf{d}) = \int_{\mathcal{B}} \mathbf{B}^T \hat{\boldsymbol{\tau}} dV; \quad (29a)$$

$$\mathbf{N}^F(\mathbf{p}) = - \int_{\mathcal{B}} \mathbf{b}^T (N^p \mathbf{p} + N_r^p \mathbf{p}_r) J dV; \quad (29b)$$

$$\mathbf{F}_{EXT} = \int_{\mathcal{B}} \rho_0 N^{\phi T} \mathbf{G} dV + \int_{\partial \mathcal{B}} N^{\phi T} \mathbf{t} dA. \quad (29c)$$

223 The quantity $\hat{\boldsymbol{\tau}} = \{\tau_{11}, \tau_{22}, \tau_{33}, \tau_{12}, \tau_{23}, \tau_{13}, \}^T$ is the vector containing the components of the sym-
 224 metric Kirchhoff effective stress and $\rho_0 = J\rho$ is the reference mass density of the soil water-
 225 mixture. $\mathbf{B} = [\mathbf{B}_1, \mathbf{B}_2, \dots, \mathbf{B}_{NQ}]$ is the classical strain-displacement matrix in spatial form, with \mathbf{B}_A
 226 ($A = 1, \dots, NQ$)

$$\mathbf{B}_A = \begin{bmatrix} N_{A,1}^{\phi} & 0 & 0 \\ 0 & N_{A,2}^{\phi} & 0 \\ 0 & 0 & N_{A,3}^{\phi} \\ N_{A,2}^{\phi} & N_{A,1}^{\phi} & 0 \\ 0 & N_{A,3}^{\phi} & N_{A,2}^{\phi} \\ N_{A,3}^{\phi} & 0 & N_{A,1}^{\phi} \end{bmatrix}.$$

228 Matrix \mathbf{b} is given by the product $\mathbf{b} = \mathbf{m}^T \mathbf{B}$, where $\{\mathbf{m}\} = \{1, 1, 1, 0, 0, 0\}^T$ for $n_{sd} = 3$, and $\mathbf{G} \equiv \mathbf{g}$ is
 229 the gravity acceleration vector.

230 Time integration of the mass balance equation (Eq. (23)) leads to

$$231 \quad \Delta t H_{\Delta t}^h(\phi, p, \tilde{\boldsymbol{\psi}}) = -\tilde{\boldsymbol{\psi}}^T [\mathbf{J}(\mathbf{d}) + \Delta t \boldsymbol{\Phi}(\mathbf{p}) + \Delta t \mathbf{H}_{EXT}] = \mathbf{0}, \quad (30)$$

232 with

$$\mathbf{J}(\mathbf{d}) = - \int_{\mathcal{B}} \mathbf{N}^{PT} (J_{n+1} - J_n) dV; \quad (31a)$$

$$\Phi(\mathbf{p}) = \beta \int_{\mathcal{B}} \mathbf{E}^T J_{n+1} \tilde{\mathbf{v}}_{n+1} dV + (1 - \beta) \int_{\mathcal{B}} \mathbf{E}_n^T J_n \tilde{\mathbf{v}}_n dV; \quad (31b)$$

$$\mathbf{H}_{EXT} = \int_{\partial\mathcal{B}} \mathbf{N}^{PT} [\beta \mathbf{Q}_{n+1} + (1 - \beta) \mathbf{Q}_n] dA, \quad (31c)$$

233 where \mathbf{N}^{PT} is the shape function matrix for the pressure field, $\mathbf{E} = [\mathbf{E}_1, \mathbf{E}_2, \dots, \mathbf{E}_{NP}]$ the gradient-
 234 pressure transformation matrix, with \mathbf{E}_A ($A = 1, \dots, NP$)

$$235 \quad \mathbf{E}_A = \text{grad } N_A^p = \begin{bmatrix} N_{A,1}^p \\ N_{A,2}^p \\ N_{A,3}^p \end{bmatrix}.$$

236 By adopting the implicit Eulero scheme ($\beta = 1$), which is first order accurate and unconditionally
 237 stable, and referring to Darcy's velocity, $\tilde{\mathbf{v}}$ (Eq (31b)) can be rewritten as

$$238 \quad \Phi(\mathbf{p}) = - \int_{\mathcal{B}} \mathbf{E}^T \frac{\mathbf{k}_{n+1}}{g \rho_F} [\mathbf{E} \{\mathbf{p} + \mathbf{p}_r\}_{n+1} - \rho_F \mathbf{g}] J_{n+1} dV, \quad (32)$$

239 with \mathbf{k} non-linear permeability tensor and $\{\mathbf{p} + \mathbf{p}_r\}$ vector of prescribed and unknown nodal pore
 240 pressures. For sake of brevity the reader is referred to (Borja and Alarc3n 1995; Borja et al. 1998)
 241 for the discretized expression of G^h and $H_{\Delta t}^h$. Particularly, the first variation of G is:

$$242 \quad \delta G^h(\phi, p, \tilde{\boldsymbol{\eta}}) = \tilde{\boldsymbol{\eta}}^T [\mathbf{K}_{\phi\phi} \delta \mathbf{d} + \mathbf{K}_{\phi p} \delta \mathbf{p}], \quad (33)$$

243 where

$$\mathbf{K}_{\phi\phi} = \int_{\mathcal{B}} [\mathbf{Z}^T \mathbf{a} \mathbf{Z} + \mathbf{Z}^T (J \mathbf{I}_p) \mathbf{Z} - \rho_F J N^{\phi T} \mathbf{G} \mathbf{b}] dV ; \quad (34a)$$

$$\mathbf{K}_{\phi p} = - \int_{\mathcal{B}} \mathbf{b}^T N^p J dV . \quad (34b)$$

244 $\mathbf{Z} = [\mathbf{Z}_1, \mathbf{Z}_2, \dots, \mathbf{Z}_{NQ}]$ is the full spatial gradient operator (see (de Souza Neto et al. 2011)), with
 245 components \mathbf{Z}_A ($A = 1, \dots, NQ$)

$$246 \quad \mathbf{Z}_A = \begin{bmatrix} N_{A,1}^{\phi} \mathbf{1} \\ N_{A,2}^{\phi} \mathbf{1} \\ N_{A,3}^{\phi} \mathbf{1} \end{bmatrix}$$

247 where $\mathbf{1}$ is the second order identity tensor, with 3×3 dimension for $n_{sd} = 3$. The quantity \mathbf{a} is the
 248 total tangent operator defined by

$$249 \quad \mathbf{a} = \mathbf{c} + (\boldsymbol{\tau} \oplus \mathbf{1}) = \boldsymbol{\alpha} - (\boldsymbol{\tau} \ominus \mathbf{1}), \quad (35)$$

250 where $\boldsymbol{\alpha}$ is the algorithmic tangent operator (Borja 2013)

$$\begin{aligned} \boldsymbol{\alpha} &= \sum_{A=1}^3 \sum_{B=1}^3 a_{AB}^{ep} \mathbf{m}^{(A)} \otimes \mathbf{m}^{(B)} \\ &\quad \sum_{A=1}^3 \sum_{B \neq A}^3 \left(\frac{\tau_B - \tau_A}{\lambda_B^{etr} - \lambda_A^{etr}} \right) (\lambda_B^{etr} \mathbf{m}^{(AB)} \otimes \mathbf{m}^{(AB)} + \lambda_A^{etr} \mathbf{m}^{(AB)} \otimes \mathbf{m}^{(BA)}), \end{aligned} \quad (36)$$

251 with $\mathbf{m}^{(A)} = \mathbf{n}^{(A)} \otimes \mathbf{n}^{(A)}$, and $\mathbf{m}^{(AB)} = \mathbf{n}^{(A)} \otimes \mathbf{n}^{(B)}$ with \mathbf{n} (Eq. (8)). λ_A^{etr} is the trial elastic principal
 252 stretch and $a_{AB}^{ep} = \partial \tau_A / \partial \varepsilon_B$ (Borja and Tamagnini 1998) is the elastoplastic tangential modulus,
 253 obtained from the *return mapping* algorithm for determining the tensor $\boldsymbol{\tau}$.

254 \mathbf{I}_p is provided by the second and third integrals of Eq. (44), and gives

$$255 \quad \mathbf{I}_p = p^h (\mathbf{1} \ominus \mathbf{1} - \mathbf{1} \otimes \mathbf{1}) . \quad (37)$$

256 then Eq. (30) holds

$$257 \quad \Delta t \Delta H_{\Delta t}^h(\phi, p, \tilde{\psi}) = -\tilde{\psi}^T [\mathbf{K}_{p\phi} \delta \mathbf{d} + \mathbf{K}_{pp} \delta \mathbf{p}], \quad (38)$$

258 where

$$\begin{aligned} \mathbf{K}_{p\phi} = & - \int_{\mathcal{B}} J N^{pT} \mathbf{b} dV - \beta \Delta t \int_{\mathcal{B}} \mathbf{E}^T \left(\frac{\mathbf{k} + \mathbf{k}' J}{\rho_F g} \right) (\mathbf{E}\{\mathbf{p} + \mathbf{p}_r\} - \rho_F \mathbf{g}) \mathbf{b} J dV \\ & + \frac{\beta \Delta t}{\rho_F g} \int_{\mathcal{B}} \mathbf{E}^T (\mathbf{A} + \mathbf{W}) \mathbf{Z} J dV; \end{aligned} \quad (39a)$$

$$\mathbf{K}_{pp} = - \frac{\beta \Delta t}{\rho_F g} \int_{\mathcal{B}} \mathbf{E}^T \mathbf{k} \mathbf{E} J dV. \quad (39b)$$

259 \mathbf{k}' operator is the first variation of the permeability tensor with respect to the Jacobian J of the
260 deformation gradient \mathbf{F} . \mathbf{A} has 3×9 dimension

$$261 \quad \mathbf{A} = [\hat{v}_1 \mathbf{1}, \hat{v}_2 \mathbf{1}, \hat{v}_3 \mathbf{1}], \quad (40)$$

262 where \hat{v}_i are the components of the vector $\hat{\mathbf{v}} = \mathbf{k} \cdot (\mathbf{E}\{\mathbf{p} + \mathbf{p}_r\} - \rho_F \mathbf{g})$. $\mathbf{W} = [\mathbf{W}_1, \mathbf{W}_2, \mathbf{W}_3]$ has 3×9
263 dimension as well

$$264 \quad \mathbf{W}_1 = \begin{bmatrix} w_{111} & w_{121} & w_{131} \\ w_{211} & w_{221} & w_{231} \\ w_{311} & w_{321} & w_{331} \end{bmatrix}$$

$$265 \quad \mathbf{W}_2 = \begin{bmatrix} w_{112} & w_{122} & w_{132} \\ w_{212} & w_{222} & w_{232} \\ w_{312} & w_{322} & w_{332} \end{bmatrix}$$

$$267 \quad \mathbf{W}_3 = \begin{bmatrix} w_{113} & w_{123} & w_{133} \\ w_{213} & w_{223} & w_{233} \\ w_{313} & w_{323} & w_{333} \end{bmatrix}$$

269 where the components are obtained from $w_{ijk} = k_{ik} p_{,j}$.

270 The final discretized coupled system of equations can be written as

$$271 \begin{Bmatrix} \mathbf{r}_\phi(\mathbf{d}, \mathbf{p}) \\ \mathbf{r}_p(\mathbf{d}, \mathbf{p}) \end{Bmatrix} = \begin{Bmatrix} \mathbf{N}^S(\mathbf{d}) \\ \mathbf{J}(\mathbf{d}) \end{Bmatrix} + \begin{Bmatrix} \mathbf{N}^F(\mathbf{p}) \\ \beta_0 \Delta t \Phi(\mathbf{p}) \end{Bmatrix} + \begin{Bmatrix} -\mathbf{F}_{EXT} \\ \beta_0 \Delta t \mathbf{H}_{EXT} \end{Bmatrix} = \begin{Bmatrix} \mathbf{0} \\ \mathbf{0} \end{Bmatrix}, \quad (41)$$

272 and the Newton-Raphson incremental solution is calculated from

$$273 \begin{bmatrix} K_{\phi\phi} & K_{\phi p} \\ K_{p\phi} & K_{pp} \end{bmatrix}_k \begin{Bmatrix} \delta \mathbf{d} \\ \delta \mathbf{p} \end{Bmatrix}_{k+1} = \begin{Bmatrix} \mathbf{r}_\phi \\ \mathbf{r}_p \end{Bmatrix}_k. \quad (42)$$

274 The tangent operator \mathbf{K} in Eq. (42) is in general non-symmetric and indefinite.

275 VALIDATION OF THE NUMERICAL CODE

276 The numerical analyses are performed by using *GeoMatFEM*, a Matlab research code for three-
277 dimensional coupled geomechanical simulations.

278 The code has been validated against two numerical examples (Borja et al. 1998), namely the
279 uniform consolidation of a soil column and the consolidation of a strip foundation. Both numerical
280 simulations assume fully saturated hyperelastic-plastic porous media.

281 Additionally, two experimental tests have been considered for validating the constitutive model.

282 Hyperelastic-plastic consolidation of a column

283 Let's consider a column of fully saturated soil with square base of 1 m side and 5 m height, as
284 shown in Fig. 4. The mesh is composed by 10 three-dimensional finite elements.

285 The material parameters are in shown in Table 1.

286 The initial stress configuration is not stress-free, but it balances the gravity load (Borja et al.
287 1998; Borja and Tamagnini 1998); it is obtained by an uncoupled small strain analysis, applying
288 self-weight in three steps and then determining the internal stresses. We recall that nonzero initial
289 stresses are required to activate the procedure, so a small initial value p_0 and preconsolidation
290 pressure p_{c0} have been assumed at all Gauss points for the first run of the model.

291 The displacements are subsequently reinitialized to zero, and the consolidation analysis is carried

292 out by applying a vertical downward load $\Delta w = 0.09$ MPa at the top of the soil column in three equal
 293 time steps at a constant rate of 0.03 MPa/day, while time steps are increased $t_{n+1} = 1.5\Delta t_n$. The
 294 results of the consolidation analysis are shown in Figs. 5(a) and 5(b) in terms of total fluid potential
 295 and average degree of consolidation versus time, respectively. The total fluid potential $\Pi = \Pi^p + \Pi^e =$
 296 $p/(\rho_w g) + x_z$ is calculated at the Gauss point A , with $X_{PGA} = [0.106 \text{ m } 0.106 \text{ m } 0.106 \text{ m}]$ close
 297 to the column base. The average degree of consolidation \bar{U}_{ave} and the time factor T are computed
 298 as

$$299 \quad \bar{U}_{ave} = \frac{\bar{u}_z(t)}{\bar{u}_z(\infty)} \quad T = \frac{c_v t}{H_0^2} = \frac{\mu_0 k}{\rho_w g} \frac{t}{H_0^2}. \quad (43)$$

300 Fig. 6 reports the isochrones of Cauchy pore pressure predicted by the small strains and finite
 301 strains approaches; the obtained results are superimposed to those reported in (Borja et al. 1998),
 302 so proving the correctness of the implemented procedure.

303 The convergence velocity (Fig. 7) exhibits a quadratic profile, typical of Newton-Raphson
 304 schemes, so configuring on this side the correct implementation of the tangent operator.

305 **Hyperelastic-plastic footstrip consolidation**

306 The consolidation of an half-space of clay subjected to a flexible footing strip (Fig. 8(a)) has
 307 been additionally considered following (Borja et al. 1998).

308 A constant value of total potential equal to $\Pi = 20.0$ m is applied, together with an initial hydrostatic
 309 Cauchy pore pressure distribution as shown in Fig. 8(b).

310 The material data of the clay are the same as in the previous example but the porosity and
 311 permeability parameters change with the deformation of the porous matrix. The material properties
 312 are reported in Table 2, assuming an hyperelastic behavior for sand and and hyperelastic-plastic
 313 one for clays.

314 Three preloading stages (case #1, case #2 and case #3) have been considered, leading to different
 315 initial stress states, similarly to what performed in the previous example. For case #1 an initial
 316 stress state due to the self-weight has been considered, while for case #2 and #3 both self-weight
 317 and two preloading conditions have been assumed, equal to 0.015 MPa and 0.030 MPa, producing

318 two different over-consolidation states. Fig. 9(a) shows the evolution of vertical displacements for
319 a node on top surface located on the symmetry plane. Fig. 9(b) depicts the evolution of Cauchy
320 pore pressure $p = \theta/J$ at Gauss point B with $X_{PGB} = [0.106 \text{ m } 0.106 \text{ m } 16.211 \text{ m}]$.

321 Again, as observed in the previous example, the results are superimposed to the benchmark
322 ones and the convergence velocity shows a quadratic profile (Fig. 10).

323 **Experimental tests**

324 The constitutive model has been further validated against an isotropic compression test and a
325 standard drained triaxial test (Callari et al. 1998; Al-Tabbaa 1987); the material parameters are
326 listed in Table 3.

327 *Isotropic compression test*

328 A normally consolidated sample with initial isotropic pressure $p_0 = p_{c0} = 0.1 \text{ MPa}$ has been
329 reconstructed and a set of loading-unloading cycles has been applied. Figure 11 depicts the
330 evolution of the specific volume v with Kirchhoff isotropic pressure P , evidencing the agreement
331 between numerical results and experimental data, both in the loading and in the unloading stages.

332 *Drained triaxial test*

333 A normally consolidate sample is now subjected to an initial isotropic pressure $p_0 = p_{c0} =$
334 0.3 MPa . The soil has been loaded in order to reach a deviatoric stress $Q = 0.12 \text{ MPa}$ and then
335 unloaded. Again, by considering Fig. 12, the real material response appears to be correctly caught
336 by the numerical model.

337 **THREE-DIMENSIONAL ANALYSIS**

338 A consolidation process due to the filling of two tall silos over a fully saturated clay domain is
339 considered.

340 Most foundation failures in clayey soils occur when a silo is quickly loaded for the first time.
341 The rapid filling process leads to a possibly hazardous increase in pore water pressure, so repro-
342 ducing a typical undrained condition associated to a decrease in effective stress, with eventual large

343 irreversible strains and possible mechanical failure (Dogangun et al. 2009) (Fig. 13). Water over-
344 pressure hinders soil compaction and causes dangerous shear deformations that could compromise
345 the structural stability.

346 The investigated example has been inspired by the case study presented in (Puzrin et al. 2010). The
347 example describes the soil behavior underneath two adjacent silos built in the Red River Valley,
348 Canada, which did not have strength enough to resist to the applied loads. The two silos were too
349 close, and therefore pressure bulbs under the foundations overlapped. This caused large stresses
350 and, in turn, large settlements under the parts of the ring foundations. The final result was tilting
351 and touching.

352 This proposed example, although simple and straightforward, is particularly suitable to investigate
353 the potentiality of the approach, and specifically to evaluate the effects of a finite strains assumption
354 on the modeled scenario. In fact, this geomechanical problem is of interest: a three-dimensional
355 simulation is required, furthermore both material and geometric non-linearities must be taken into
356 account, along with the interaction between solid and fluid phases. Additionally, as reported below,
357 even the so called $P - \Delta$ effect can be caught thanks only to the introduced geometric non linearity.

358 Two cylindrical silos with 10 m diameter, 40 m height and placed at a distance of 2 m m one
359 to the other (Fig. 14) have been reconstructed. The silos are built on a normally consolidated and
360 fully saturated clay layer of 30 m, resting on a rigid rock base. In order to reduce the number of
361 elements, only half of the model has been realized, to take advantage of the symmetry with respect
362 to the $X-Z$ plane. Lateral surfaces are assumed to be horizontally restrained with the bottom surface
363 fixed; free flux can occur on top and bottom of the clay layer.

364 The soil discretization is composed by 3542 D20P8 mixed finite elements, with a total of 3622
365 elements, with 16644 nodes for the displacement field, 4356 of which also for the pore pressure
366 field; the total degrees of freedom are 54288.

367 As previously done, an initial stage accounting for the self-weight, plus a surface pressure $p_i =$
368 0.2 MPa, has been considered.

369 By assuming that the silos are used for the storage of cereals, a load of 0.8 t/m^3 is added

370 to the consolidation analysis. The silos are modeled as rigid elastic elements (Young's modulus
371 $E = 1 \times 10^4 \text{MPa}$ and Poisson ratio $\nu = 0$). Permeability k is calculated via the Kozeny-Carman
372 equation (Eq. 18), whereas for the small strain analysis the value indicated in Table 4 applies.

373 The two silos are simultaneously filled during four constant time steps of 12 h, then the weight is
374 maintained during the consolidation stage. The time steps are increased according to the equation:
375 $\Delta t_{n+1} = 1.5 \Delta t_n$. Fig. 15 shows the time evolution of the vertical displacements for the central point
376 of the silos base (points C and D of Fig. 14), evidencing pretty similar results when small or
377 finite strains are considered: particularly, a difference of 0.9 % in the final settlements have been
378 obtained; when horizontal displacements of top of silos are taken into account (Fig. 16, points A
379 and B), the difference reaches 68 % and the silos rotation predicted by the finite strains analysis
380 is about three times higher (1.56°) than that reported by the small strains one. Such a difference
381 evidences the $P - \Delta$ contribution, essential in the correct description of the ultimate scenario.

382 Correspondingly, the represented situation is particularly hazardous, implying that the silos under
383 such a rotation can come into contact (at approximately 90 days when the analysis is then stopped).

384 Fig. 17 shows the evolution of Cauchy pore pressure at points E and F (Fig. 14), i.e. 3 m
385 below the top of clay layer. After the fast filling of the two silos, the pore pressure reaches the
386 maximum peak value of 0.26 MPa for both small and finite strains analysis (typical undrained
387 condition). Since initially the load is sustained by the pore pressure, the skeleton does not deform,
388 and therefore the two models give a very similar result in terms of pressure peak. Further, with the
389 evolution of pore pressure in time (drained condition), the results show a slightly lower rate of pore
390 pressure if finite strains are accounted for, due to the change in permeability with soil deformation.
391 The final value of pore pressure is hence of 0.031 MPa, slightly higher than the initial hydrostatic
392 pressure of 0.030 MPa. This is the consequence of imposing a constant hydraulic potential at the
393 bottom of the clay layer, and represents a local artesian condition due to the deformation of the soil.
394 Finally, an overview of pore pressure evolution in finite strains regime is visible in Fig. 18, which
395 shows the contours of Cauchy pore pressure for some time steps. The typical consolidation bulbs
396 is evidenced under the two silos, which slowly dissipates until the initial hydrostatic condition is

397 reached (Fig. 18.f).

398 The results in terms of plastic deformations are plotted in Figs. 19 and 20. Both analyses give
399 similar values but those from finite strains model are higher, plus a wider zone of soil plasticization
400 between the two silos, producing in turn a differential settlement at silos' foundation $\Delta u_z = 26.4$ cm
401 ($\Delta u_z = 8.5$ cm for the small strain model). By considering Fig. 20, it is interesting to observe two
402 conical zones characterized by high deviatoric plastic deformations, resembling hence typical 3D
403 shear bands of strain localization.

404 Fig. 21 depicts the plastic deformations plotted along vertical Z-Z axis (see Fig. 14), evidencing
405 the relevance of a finite strains approach. Both volumetric and deviatoric strains show their peak in
406 proximity of the silos' foundation, with a deformation mechanism essentially of deviatoric nature,
407 as reported below. Finally, Fig. 22 plots the P–Q stress path for Gauss points G (see Fig. 14),
408 showing no appreciable differences in terms of stress for small and finite strains analyses. Figs. 23
409 evidences that, even if the predicted volumetric stress is always higher than the deviatoric one, the
410 deformation mechanism is mainly driven by deviatoric strains in the undrained stage (*I*; higher
411 deviatoric strains and higher deviatoric strain rate) and by volumetric strains in the drained stage
412 (*II*; consolidation, higher volumetric strain rate). Anyway, overall larger deviatoric strains (as
413 reported by Fig. 21) show a typical soil behaviour more sensitive to shear straining, a mechanism
414 appreciable via a finite strains approach only.

415 CONCLUSIONS

416 In this work a fully coupled hydro-mechanical model has been described and validated against
417 available literature and experimental results. Particularly, the model has been developed within a 3D
418 Finite Element research code by assuming material and geometric non-linearities, also introducing
419 a dependence of permeability on deformation as well as a specific type of mixed finite element.
420 The former allows for correctly reproducing fully saturated scenarios in finite strains, the latter for
421 solving stability issues of the adopted formulation.

422 A consolidation case study has evidenced the potentialities of the code and the relevance of a finite
423 strains approach, particularly when $P - \Delta$ effects must be accounted for in realistically reproducing

424 hazardous scenarios of soil-structure interaction. Together with the capability of reaching such
425 an ultimate state of silos tilting, the upgraded code has even demonstrated to better describe the
426 evolution of the deformation state for the foundation soil, experiencing a transition from higher
427 deviatoric strains and higher deviatoric strain rates to higher volumetric strain rates when passing
428 from an undrained stage to a drained one.

429 **ACKNOWLEDGMENTS**

430 Financial support from the Italian Ministry of Education, University and Research (MIUR)
431 in the framework of the Project PRIN “COAN 5.50.16.01”- code 2015JW9NJT - is gratefully
432 acknowledged.

433 **APPENDIX I. FIRST VARIATION OF THE LINEAR MOMENTUM AND MASS BALANCE**
 434 **EQUATIONS**

435 The variation of the linear momentum, Eq. (21), in the spatial form is written as:

$$\begin{aligned}
 \delta G = & \int_{\mathcal{B}} \text{grad } \boldsymbol{\eta} : (\mathbf{c} + \boldsymbol{\tau} \oplus \mathbf{1}) : \text{grad } \delta \mathbf{u} \, dV \\
 & - \int_{\mathcal{B}} \text{grad } \boldsymbol{\eta} : (Jp\mathbf{1} \otimes \mathbf{1}) : \text{grad } \delta \mathbf{u} \, dV + \int_{\mathcal{B}} Jp \text{grad}^T \boldsymbol{\eta} : \text{grad } \delta \mathbf{u} \, dV \\
 & - \int_{\mathcal{B}} J \delta p \text{div } \boldsymbol{\eta} \, dV - \int_{\mathcal{B}} \rho_F J \text{div}(\delta \mathbf{u}) \boldsymbol{\eta} \cdot \mathbf{g} \, dV - \int_{\partial \mathcal{B}} \boldsymbol{\eta} \cdot \delta \mathbf{t} \, dA, \quad (44)
 \end{aligned}$$

436 where \mathbf{c} is the fourth order spatial tangent tensor (Borja and Alarcón 1995), $\boldsymbol{\tau} \oplus \mathbf{1}$ is a fourth order
 437 tensor representing the initial stress term and $Jp\mathbf{1} \otimes \mathbf{1}$ is a fourth order tensor representing the
 438 pore pressure term. The quantities $\delta \mathbf{u}$, δp and $\delta \mathbf{t}$ are the variation of the displacement vector, the
 439 Cauchy pore pressure and stress vector, respectively.

440 The first variation of mass balance, Eq. (23), integrated over a fixed Δt in the spatial configuration
 441 is:

$$\begin{aligned}
 \delta H_{\Delta t} = & \int_{\mathcal{B}} \frac{\psi}{\Delta t} J \text{div } \delta \mathbf{u} \, dV + \beta \int_{\mathcal{B}} \text{grad } \psi \cdot \frac{J \mathbf{k}}{g \rho_F} \cdot \text{grad } \delta \theta \, dV \\
 & + \beta \int_{\mathcal{B}} \text{grad } \psi \cdot \left(\frac{\mathbf{k}}{g \rho_F} + \frac{J}{g \rho_F} \frac{\partial \mathbf{k}}{\partial J} \right) \cdot [\text{grad } p - \rho_F \mathbf{g}] J \, dV \\
 & - \beta \int_{\mathcal{B}} \text{grad } \psi \cdot \text{grad } \delta \mathbf{u} \cdot \frac{\mathbf{k}}{g \rho_F} \cdot [\text{grad } p - \rho_F \mathbf{g}] J \, dV \\
 & - \beta \int_{\mathcal{B}} \text{grad } \psi \cdot \frac{J \mathbf{k}}{g \rho_F} \cdot \text{grad}^t \delta \mathbf{u} \cdot \text{grad } p \, dV - \beta \int_{\partial \mathcal{B}} \psi \delta Q \, dA, \quad (45)
 \end{aligned}$$

442 where δQ is the variation of the flux Q through the surface dA .

REFERENCES

- 443
- 444 Abe, K., Soga, K., and Bandara, S. (2013). “Material point method for coupled hydromechanical
- 445 problems.” *Journal of Geotechnical and Geoenvironmental Engineering*, 140(3), 04013033.
- 446 Al-Tabbaa, A. (1987). “Permeability and stress-strain response of speswhite kaolin.” Ph.D. thesis,
- 447 University of Cambridge, University of Cambridge.
- 448 Andresen, L., Petter Jostad, H., and Andersen, K. H. (2010). “Finite element analyses applied in de-
- 449 sign of foundations and anchors for offshore structures.” *International Journal of Geomechanics*,
- 450 11(6), 417–430.
- 451 Armero, F. (1999). “Formulation and finite element implementation of a multiplicative model of
- 452 coupled poro-plasticity at finite strains under fully saturated conditions.” *Computer Methods in*
- 453 *Applied Mechanics and Engineering*, 171(3-4), 205–241.
- 454 Arnold, D. N. (1990). “Mixed finite element methods for elliptic problems.” *Computer Methods in*
- 455 *Applied Mechanics and Engineering*, 82(1-3), 281–300.
- 456 Arnold, D. N., Brezzi, F., and Fortin, M. (1984). “A stable finite element for the stokes equations.”
- 457 *Calcolo*, 21(4), 337–344.
- 458 Atluri, S. N. and Zhu, T. (1998). “A new meshless local petrov-galerkin (mlpg) approach in
- 459 computational mechanics.” *Computational Mechanics*, 22(2), 117–127.
- 460 Bienen, B., Ragni, R., Cassidy, M. J., and Stanier, S. A. (2015). “Effects of consolidation under
- 461 a penetrating footing in carbonate silty clay.” *Journal of Geotechnical and Geoenvironmental*
- 462 *Engineering*, 141(9), 04015040.
- 463 Borja, R. I. (2013). *Plasticity*. Springer.
- 464 Borja, R. I. and Alarcón, E. (1995). “A mathematical framework for finite strain elastoplastic con-
- 465 solidation part 1: Balance laws, variational formulation, and linearization.” *Computer Methods*
- 466 *in Applied Mechanics and Engineering*, 122(1), 145–171.
- 467 Borja, R. I. and Tamagnini, C. (1998). “Cam-clay plasticity part iii: Extension of the infinitesimal
- 468 model to include finite strains.” *Computer Methods in Applied Mechanics and Engineering*,
- 469 155(1), 73–95.

470 Borja, R. I., Tamagnini, C., and Alarcón, E. (1998). “Elastoplastic consolidation at finite strain
471 part 2: finite element implementation and numerical examples.” *Computer Methods in Applied
472 Mechanics and Engineering*, 159(1), 103–122.

473 Brezzi, F. and Bathe, K.-J. (1990). “A discourse on the stability conditions for mixed finite element
474 formulations.” *Computer Methods in Applied Mechanics and Engineering*, 82(1-3), 27–57.

475 Caldwell, J. A., Ferguson, K., Schiffman, R. L., and van Zyl, D. (1984). “Application of finite
476 strain consolidation theory for engineering design and environmental planning of mine tailings
477 impoundments.” *Sedimentation Consolidation Models—Predictions and Validation*, ASCE, 581–
478 606.

479 Callari, C., Auricchio, F., and Sacco, E. (1998). “A finite-strain cam-clay model in the framework
480 of multiplicative elasto-plasticity.” *International Journal of Plasticity*, 14(12), 1155–1187.

481 Carbonell, J. M., Oñate, E., and Suárez, B. (2009). “Modeling of ground excavation with the
482 particle finite-element method.” *Journal of Engineering Mechanics*, 136(4), 455–463.

483 de Souza Neto, E. A., Peric, D., and Owen, D. R. J. (2011). *Computational methods for plasticity:
484 theory and applications*. John Wiley & Sons.

485 Dogangun, A., Karaca, Z., Durmus, A., and Sezen, H. (2009). “Cause of damage and failures in
486 silo structures.” *Journal of Performance of Constructed Facilities*, 23(2), 65–71.

487 Guzmán, J. and Sánchez, M. A. (2015). “Max-norm stability of low order taylor–hood elements in
488 three dimensions.” *Journal of Scientific Computing*, 65(2), 598–621.

489 Huang, J., Xie, X., Zhang, J., Li, J., and Wang, W. (2014). “Nonlinear finite strain consolidation
490 analysis with secondary consolidation behavior.” *Mathematical Problems in Engineering*, 2014,
491 1–8.

492 Hughes, T. J. (2012). *The finite element method: linear static and dynamic finite element analysis*.
493 Courier Corporation.

494 Kardani, M., Nazem, M., Sheng, D., and Carter, J. P. (2013). “Large deformation analysis of
495 geomechanics problems by a combined rh-adaptive finite element method.” *Computers and
496 Geotechnics*, 49, 90–99.

497 Lee, W. F., Liao, H., Chang, M., Wang, C., Chi, S., and Lin, C. (2012). "Failure analysis of a
498 highway dip slope slide." *Journal of Performance of Constructed Facilities*, 27(1), 116–131.

499 Lewis, R. W. and Schrefler, B. A. (1998). *The finite element method in the static and dynamic*
500 *deformation and consolidation of porous media*. John Wiley.

501 Marsden, J. E. and Hughes, T. J. (1994). *Mathematical foundations of elasticity*. Courier Corpora-
502 tion.

503 Meguid, M. A., Rowe, R., and Lo, K. (2002). "3d effects of surface construction over existing
504 subway tunnels." *International Journal Geomechanics*, 2(4), 447–469.

505 Mohammadi, S. and Taiebat, H. (2014). "H-adaptive updated lagrangian approach for large-
506 deformation analysis of slope failure." *International Journal of Geomechanics*, 15(6), 04014092.

507 Nazem, M., Sheng, D., and Carter, J. P. (2006). "Stress integration and mesh refinement for large
508 deformation in geomechanics." *International Journal for Numerical Methods in Engineering*,
509 65(7), 1002–1027.

510 Osman, A. S. and Randolph, M. F. (2011). "Analytical solution for the consolidation around a
511 laterally loaded pile." *International Journal of Geomechanics*, 12(3), 199–208.

512 Puzrin, A. M., Alonso, E. E., and Pinyol, N. M. (2010). *Geomechanics of failures*. Springer Science
513 & Business Media.

514 Qi, S., Simms, P., and Vanapalli, S. (2017). "Piecewise-linear formulation of coupled large-strain
515 consolidation and unsaturated flow. i: Model development and implementation." *Journal of*
516 *Geotechnical and Geoenvironmental Engineering*, 143(7), 04017018.

517 Simo, J. (1992). "Algorithms for static and dynamic multiplicative plasticity that preserve the
518 classical return mapping schemes of the infinitesimal theory." *Computer Methods in Applied*
519 *Mechanics and Engineering*, 99(1), 61–112.

520 Simo, J. and Meschke, G. (1993). "A new class of algorithms for classical plasticity extended to
521 finite strains. application to geomaterials." *Computational Mechanics*, 11(4), 253–278.

522 Singh, R. P., Ojha, C. S., Prasad, O., and Singh, M. (2016). "Finite volume approach for finite strain
523 consolidation." *International Journal for Numerical and Analytical Methods in Geomechanics*,

524 40, 117–140.

525 Song, X. and Borja, R. I. (2014). “Mathematical framework for unsaturated flow in the finite
526 deformation range.” *International Journal for Numerical Methods in Engineering*, 97(9), 658–
527 682.

528 Spiezia, N., Salomoni, V. A., and Majorana, C. E. (2016). “Plasticity and strain localization around a
529 horizontal wellbore drilled through a porous rock formation.” *International Journal of Plasticity*,
530 78, 114–144.

531 Wang, C., Wang, Y., Peng, C., and Meng, X. (2016). “Smoothed particle hydrodynamics simulation
532 of water-soil mixture flows.” *Journal of Hydraulic Engineering*, 142(10), 04016032.

533 Wang, D., Hu, Y., and Randolph, M. F. (2009). “Three-dimensional large deformation finite-element
534 analysis of plate anchors in uniform clay.” *Journal of Geotechnical and Geoenvironmental
535 Engineering*, 136(2), 355–365.

536 Wriggers, P. (2008). *Nonlinear finite element methods*. Springer Science & Business Media.

537 Zhang, J., Cui, X., Huang, D., Jin, Q., Lou, J., and Tang, W. (2015). “Numerical simulation of con-
538 solidation settlement of pervious concrete pile composite foundation under road embankment.”
539 *International Journal of Geomechanics*, 16(1), B4015006.

540 Zhang, W., Yuan, W., and Dai, B. (2018). “Smoothed particle finite-element method for
541 large-deformation problems in geomechanics.” *International Journal of Geomechanics*, 18(4),
542 04018010.

543 Zhu, H. and Randolph, M. F. (2009). “Large deformation finite-element analysis of submarine
544 landslide interaction with embedded pipelines.” *International Journal of Geomechanics*, 10(4),
545 145–152.

546

List of Tables

547

1 Material parameters for the hyperelastic-plastic MCC model. 28

548

2 Material parameters for plane strain footstrip consolidation problem. 29

549

3 Material parameters adopted for the speswhite kaolin (Callari et al. 1998; Al-Tabbaa
1987). 30

550

551

4 Material parameters for the clay layer (3D analysis). 31

TABLE 1

Parameter	U.M.	Small strains	Finite strains
μ_0	MPa	0.2	0.2
α		0.0	0.0
\tilde{k}		0.0476	-
$\tilde{\lambda}$		0.1667	-
\hat{k}		-	0.05
$\hat{\lambda}$		-	0.2
M		1.00	1.00
p_0	MPa	-0.01	-0.01
p_{c0}	MPa	-0.01	-0.01
ϵ_{v0}^e		0.00	0.00
ρ_s	t/mm ³	2.7×10^{-9}	2.7×10^{-9}
ρ_w	t/mm ³	1.0×10^{-9}	1.0×10^{-9}
φ		0.7024	0.7024
k	mm/s	1.0×10^{-5}	1.0×10^{-5}

TABLE 2

Sand layer			
Parameter	U.M.	Small strains	Finite strains
ν		0.0	0.0
φ_0		-	0.4118
ρ_s	t/mm ³	-	2.7×10^{-9}
ρ_w	t/mm ³	-	1.0×10^{-9}
ρ	t/mm ³	$2,00 \times 10^{-9}$	-

Clay layer			
Parameter	U.M.	Small strains	Finite strains
φ		0.5441	0.5441
k	mm/s	1.0×10^{-6}	1.0×10^{-6}

TABLE 3

Parameter	U.M.	Values
α		90.0
\hat{k}		0.013
$\hat{\lambda}$		0.93
M		0.80
$\epsilon_{\nu_0}^e$		0.00
ν_0		2.37

TABLE 4

Parameters	U.M.	Small strain	Finite strain
μ_0	MPa	5.0	5.0
α		0.0	0.0
\tilde{k}		0.0196	-
$\tilde{\lambda}$		0.0385	-
\hat{k}		-	0.02
$\hat{\lambda}$		-	0.04
M		1.00	1.00
p_0	MPa	-0.050	-0.050
p_{c0}	MPa	-0.050	-0.050
ϵ_{v0}^e		0.00	0.00
ρ_s	t/mm ³	2.7×10^{-9}	2.7×10^{-9}
ρ_w	t/mm ³	1.0×10^{-9}	1.0×10^{-9}
φ		0.36	0.36
k	mm/s	0.6328×10^{-5}	-
D	mm	-	1.0×10^{-3}
μ	MPa-s	-	1.0×10^{-9}

552

List of Figures

553	1	Yield Surface for the Modified Cam-Clay model and Critical State Line in the $P-Q$	
554		plane.	35
555	2	Bi-logarithmic hardening law in terms of P and v	36
556	3	The displacement-pressure coupled finite element.	37
557	4	Hyperelastic-plastic consolidation of a column (Δw is the vertical load and f	
558		indicates the free volumetric flow).	38
559	5	One-dimensional hyperelastic-plastic consolidation.	39
560	(a)	Total potential Π , at Gauss point A	39
561	(b)	Average degree of consolidation versus time factor	39
562	6	One dimensional hyperelastic-plastic consolidation: isochrones of Cauchy pore	
563		pressures.	40
564	(a)	Small strain	40
565	(b)	Finite strain	40
566	7	Convergence profile of Newton-Raphson iterations.	41
567	(a)	Small strain	41
568	(b)	Finite strain	41
569	8	Plane strain footstrip consolidation problem.	42
570	(a)	Finite element mesh. (The dark elements are the drainage sand layer, Δw is	
571		the vertical load and f indicates the free volumetric flow)	42
572	(b)	Initial pore water pressure	42
573	9	Plane strain hyperelastic-plastic consolidation. Case #1, #2 and #3 assume finite	
574		strains. Empty markers reproduce benchmark results (Borja et al. 1998).	43
575	(a)	Ground surface settlement at centerline	43
576	(b)	Cauchy pore pressure at point B	43
577	10	Convergence profile of Newton-Raphson iterations.	44
578	(a)	Small strain	44

579	(b) Finite strain	44
580	11 Isotropic compression test, comparison between FEM model and experimental data.	45
581	12 Drained triaxial test, comparison between FEM model and experimental data. . . .	46
582	(a) Stress invariants ratio versus volumetric deformation	46
583	(b) Stress invariants ratio versus deviatoric deformation	46
584	13 Examples of silos failure (Dogangun et al. 2009).	47
585	(a)	47
586	(b)	47
587	14 Finite element model of the two silos.	48
588	(a) Three-dimensional view	48
589	(b) X-Z plane view	48
590	15 Vertical displacement at the silos base.	49
591	16 Horizontal displacement with respect to the Z-Z axis.	50
592	17 Cauchy pore pressure.	51
593	18 Deformed meshes and contours of Cauchy pore pressure assuming finite strains. . .	52
594	(a) t = 48 h	52
595	(b) t = 54 h	52
596	(c) t = 92 h	52
597	(d) t = 270 h	52
598	(e) t = 1170 h	52
599	(f) t = 5730 h	52
600	19 Volumetric plastic strain at the end of consolidation analysis.	53
601	(a) Finite strain analysis	53
602	(b) Small strain analysis	53
603	20 Deviatoric plastic strain at the end of consolidation analysis.	54
604	(a) Finite strain analysis	54
605	(b) Small strain analysis	54

606	21	Plastic strain along vertical <i>Z-Z</i> axis at the end of consolidation analysis.	55
607		(a) Volumetric plastic strain	55
608		(b) Deviatoric plastic strain	55
609	22	Stress path at Gauss point G.	56
610	23	Stress - strain curves for Gauss point G.	57
611		(a) Isotropic stress versus volumetric plastic strain	57
612		(b) Deviatoric stress versus deviatoric plastic strain	57

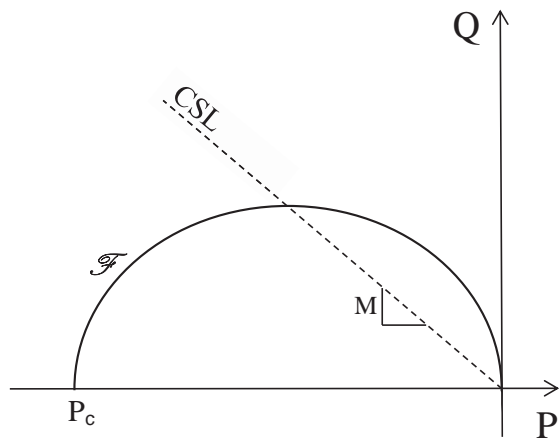


Fig. 1

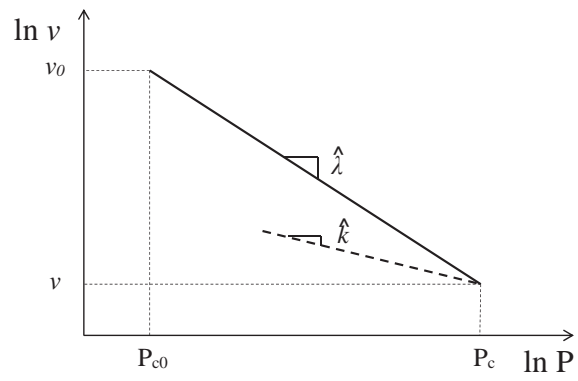


Fig. 2

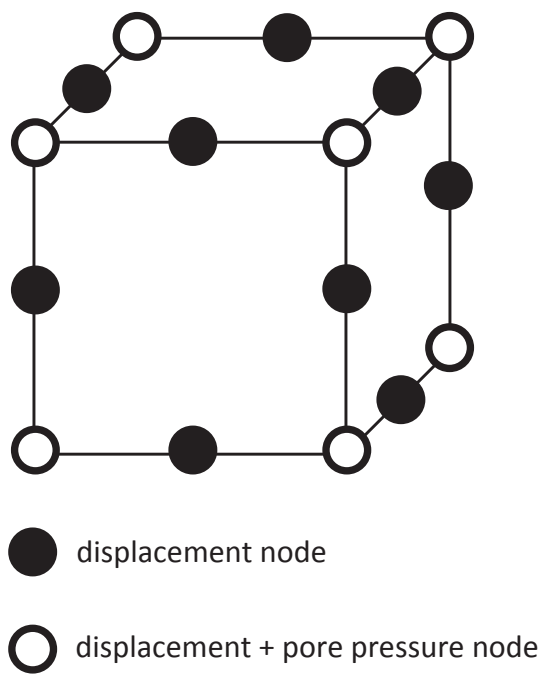


Fig. 3

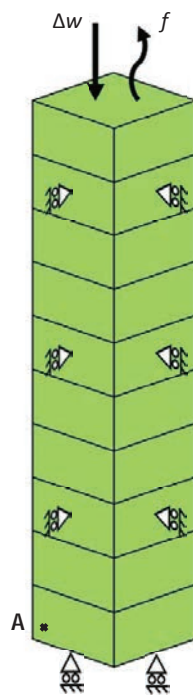
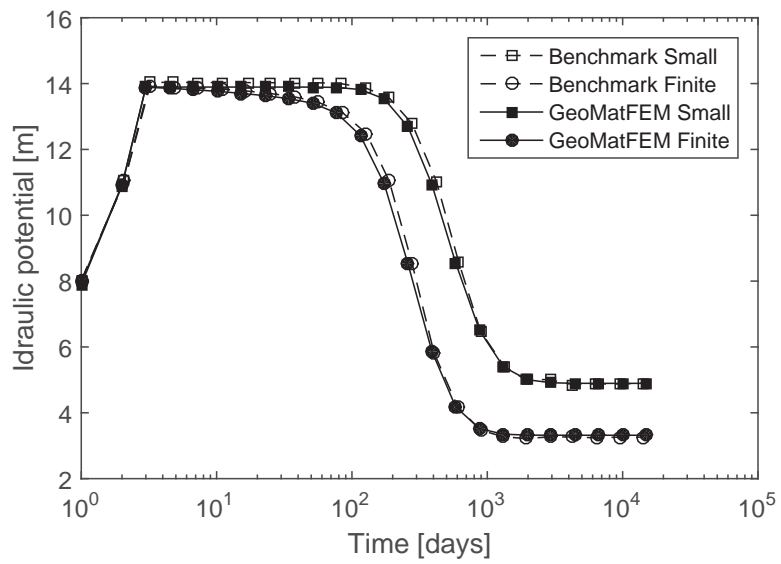
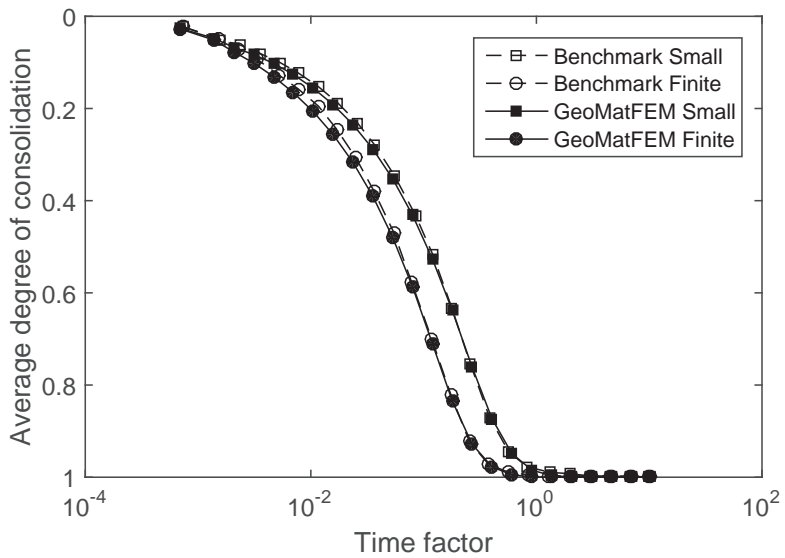


Fig. 4

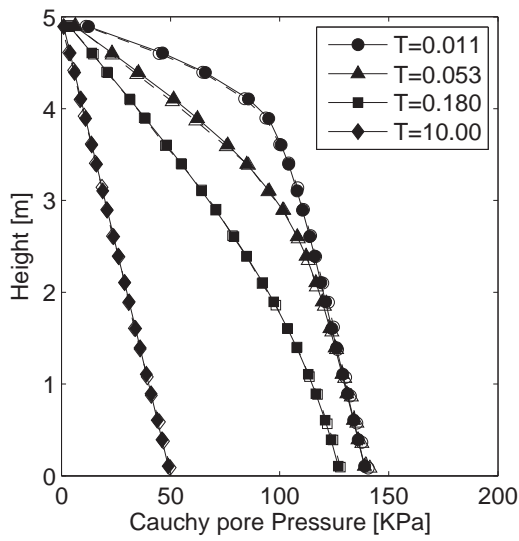


(a)

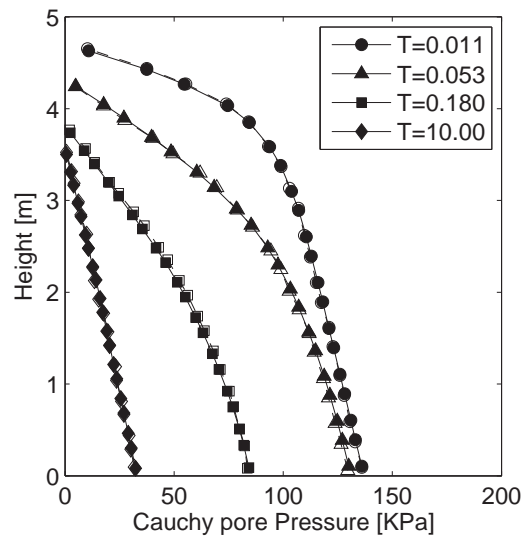


(b)

Fig. 5

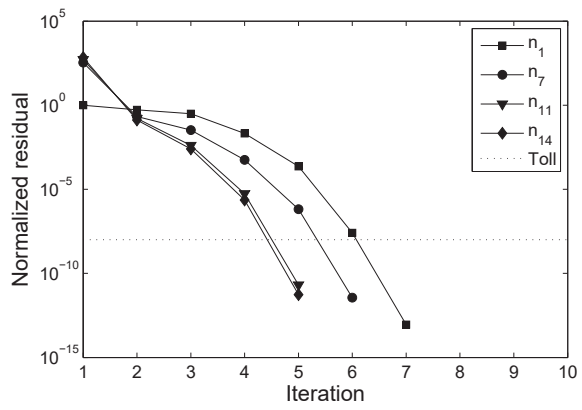


(a)

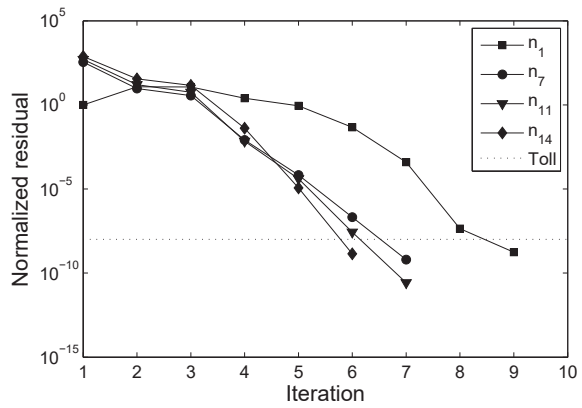


(b)

Fig. 6

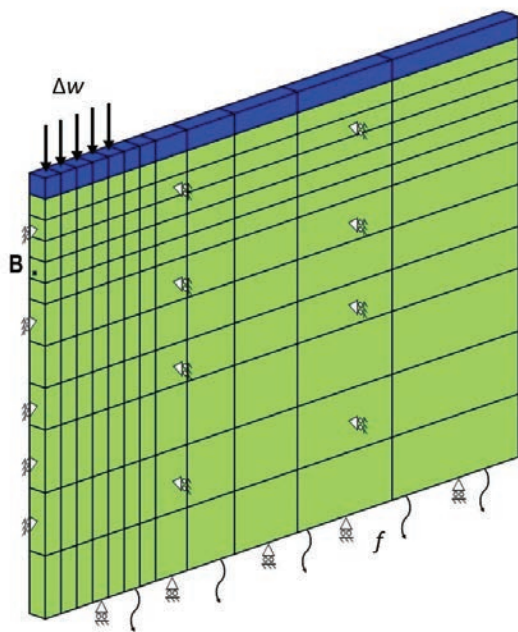


(a)

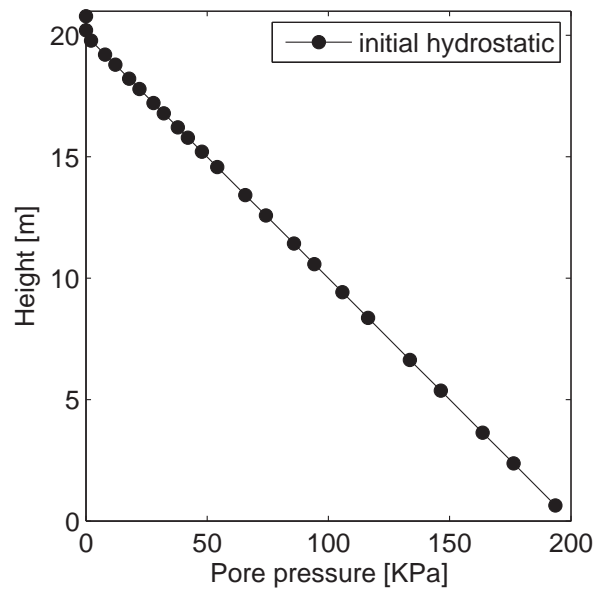


(b)

Fig. 7

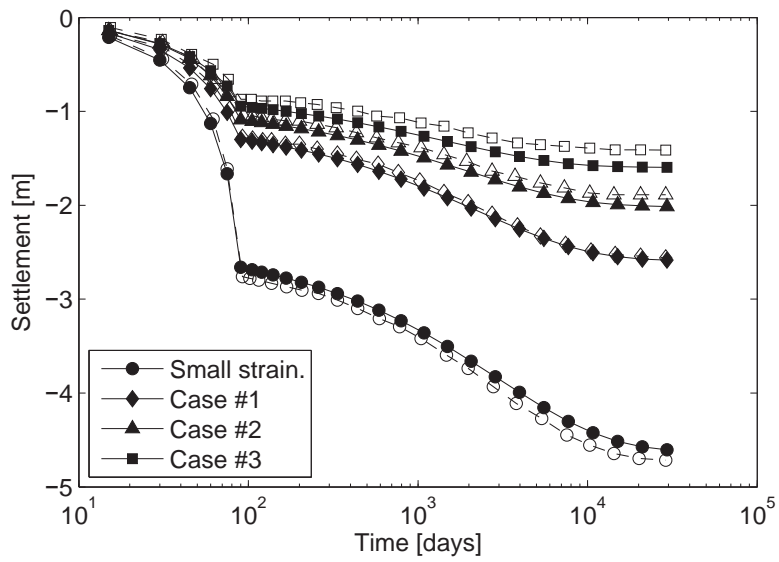


(a)

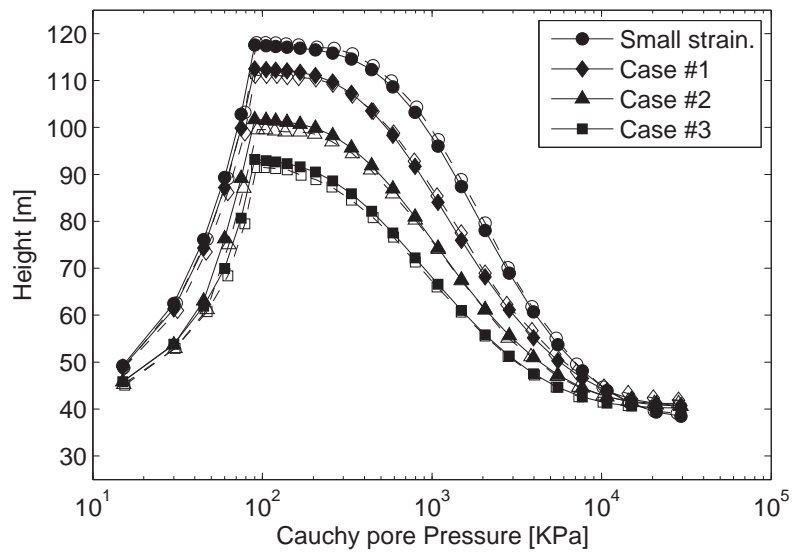


(b)

Fig. 8

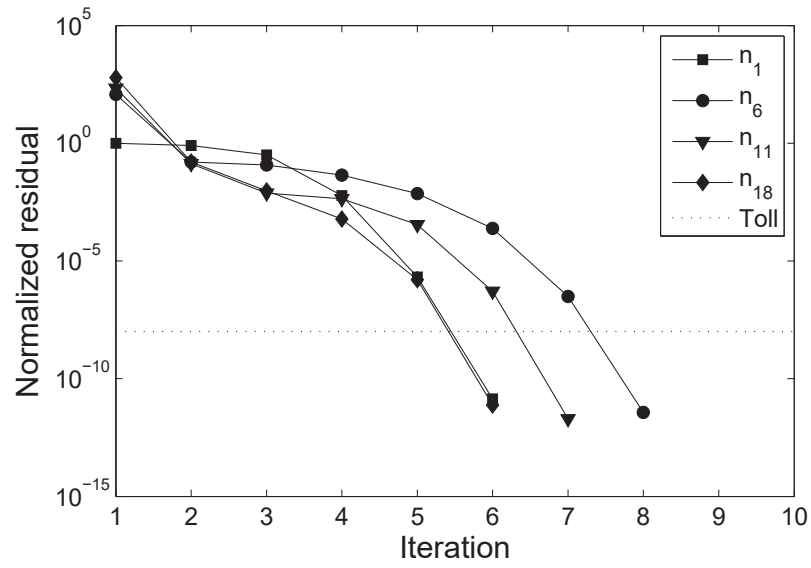


(a)

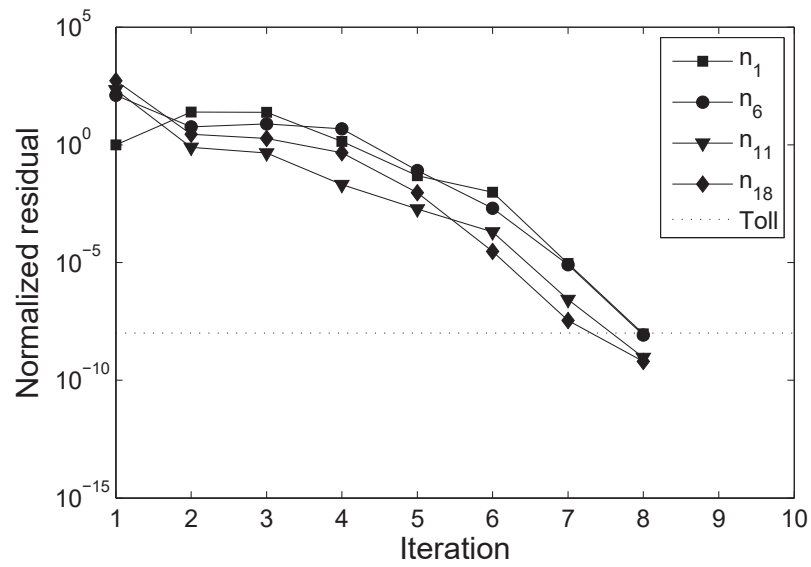


(b)

Fig. 9



(a)



(b)

Fig. 10

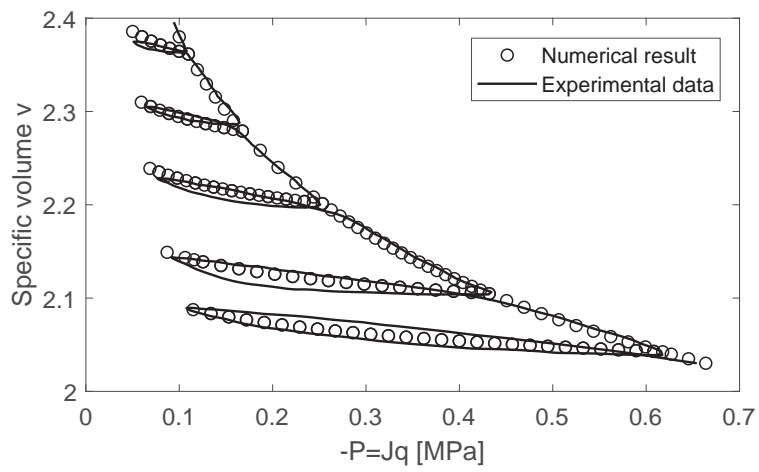
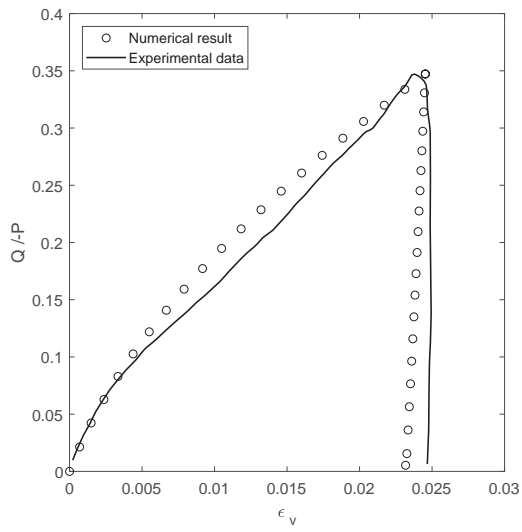
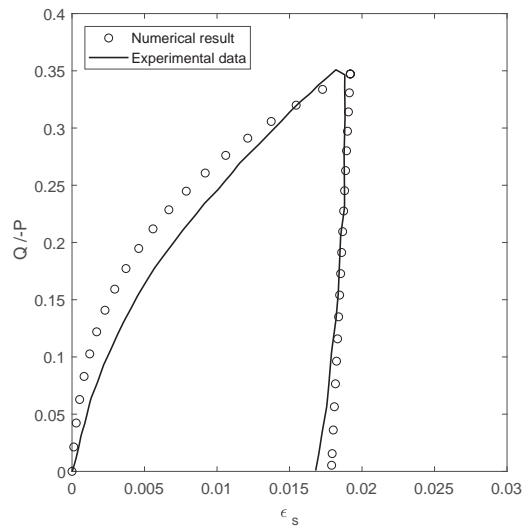


Fig. 11



(a)

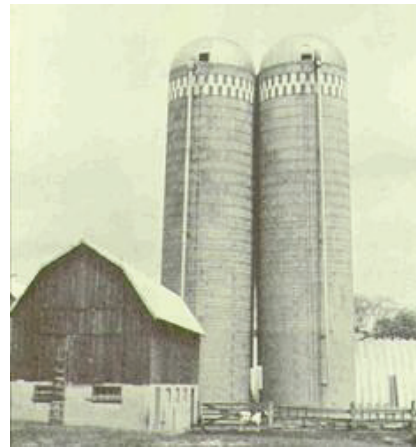


(b)

Fig. 12



(a)



(b)

Fig. 13

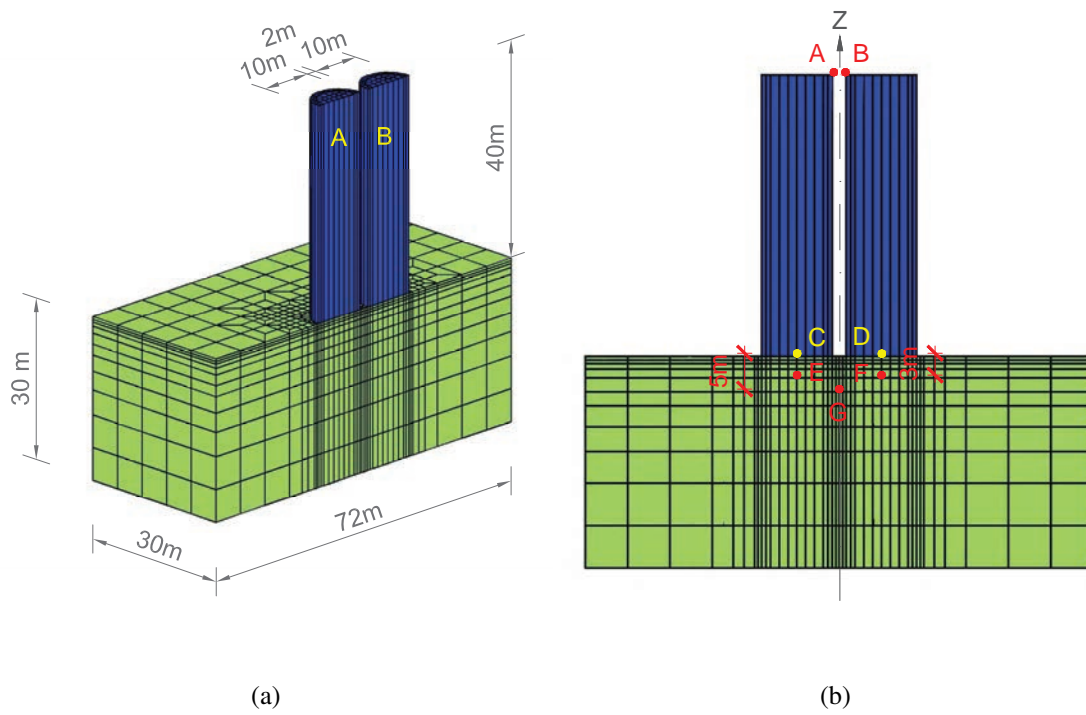


Fig. 14

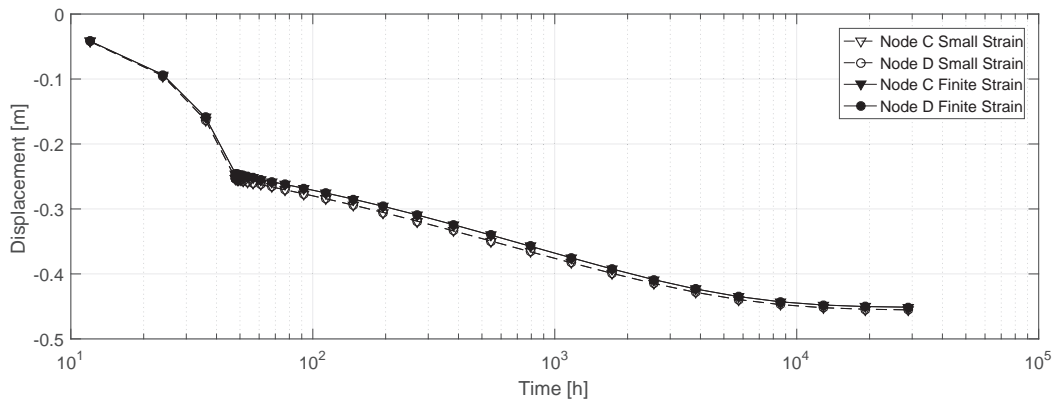


Fig. 15

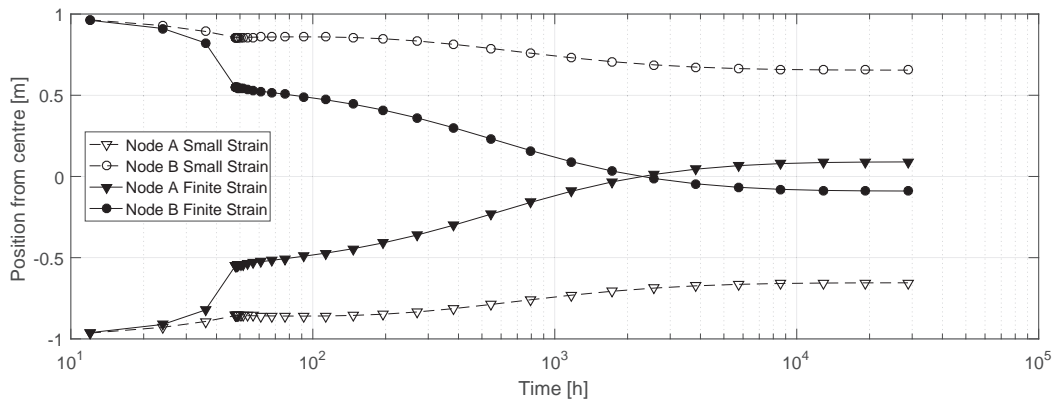


Fig. 16

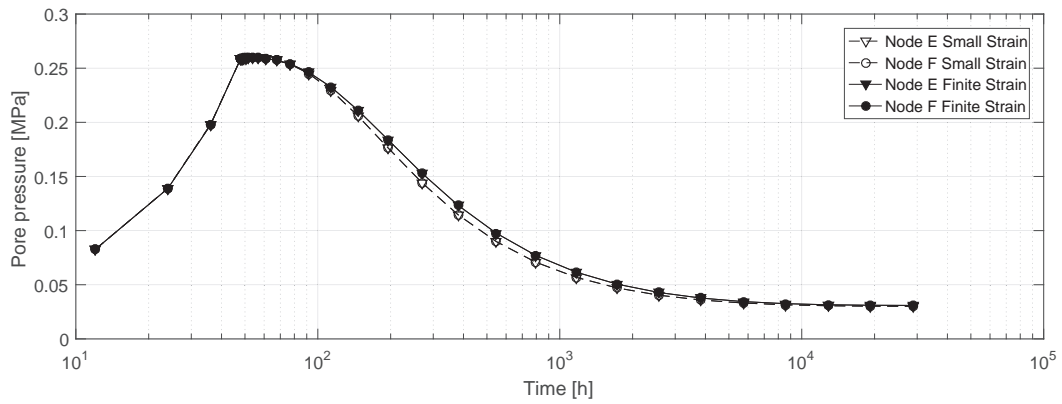
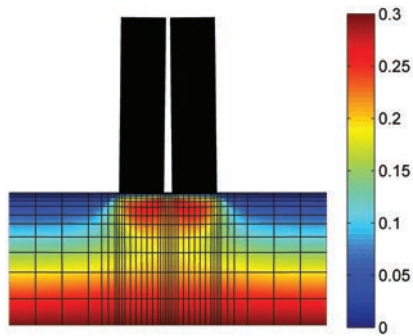
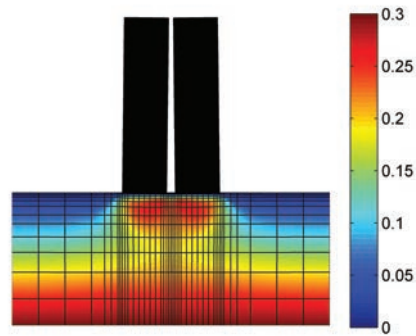


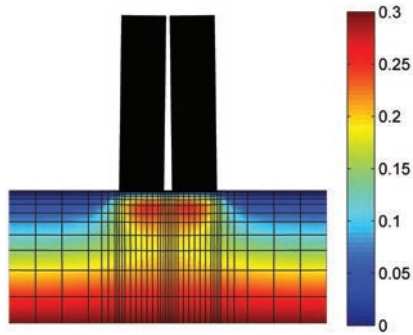
Fig. 17



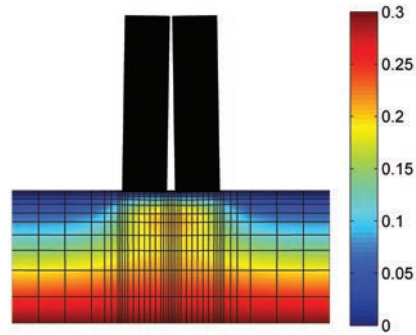
(a)



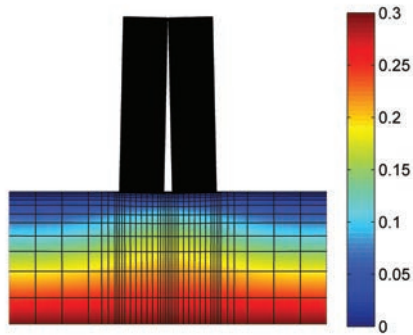
(b)



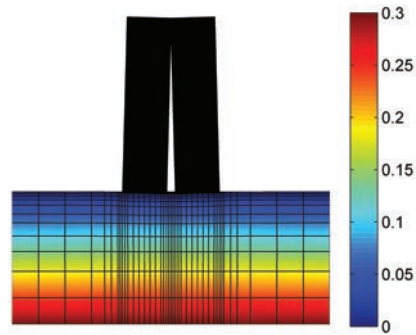
(c)



(d)

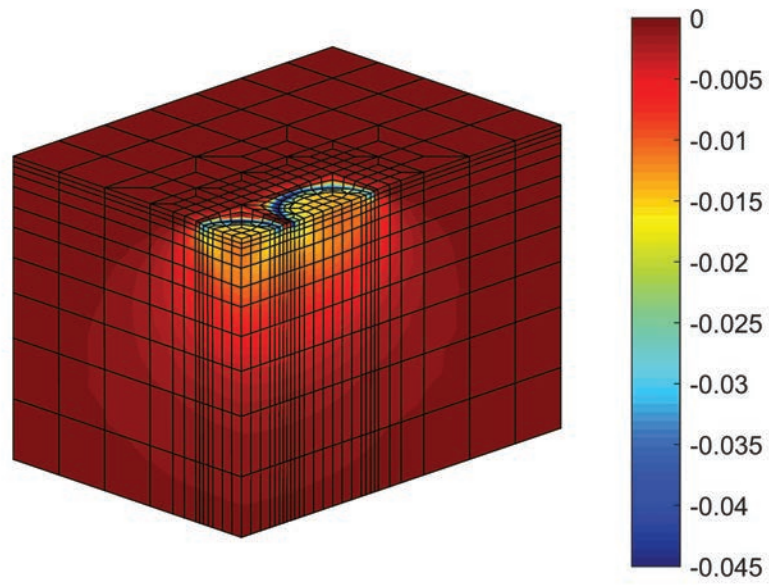


(e)

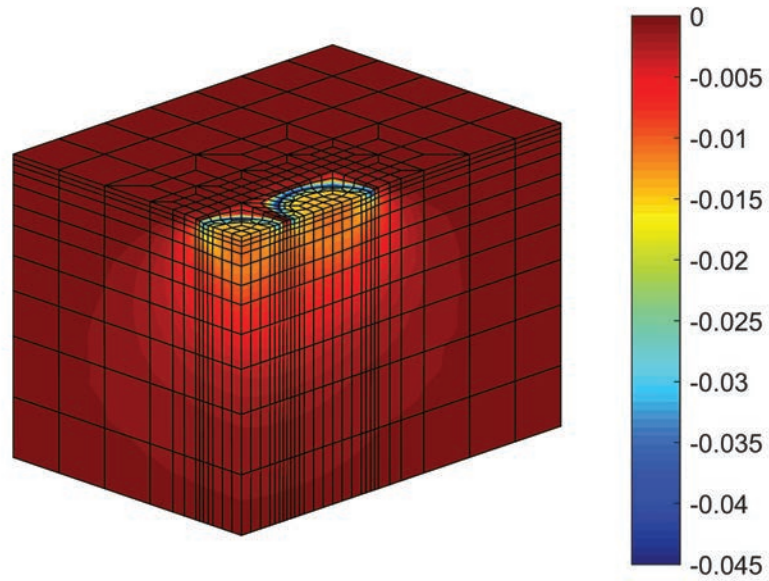


(f)

Fig. 18

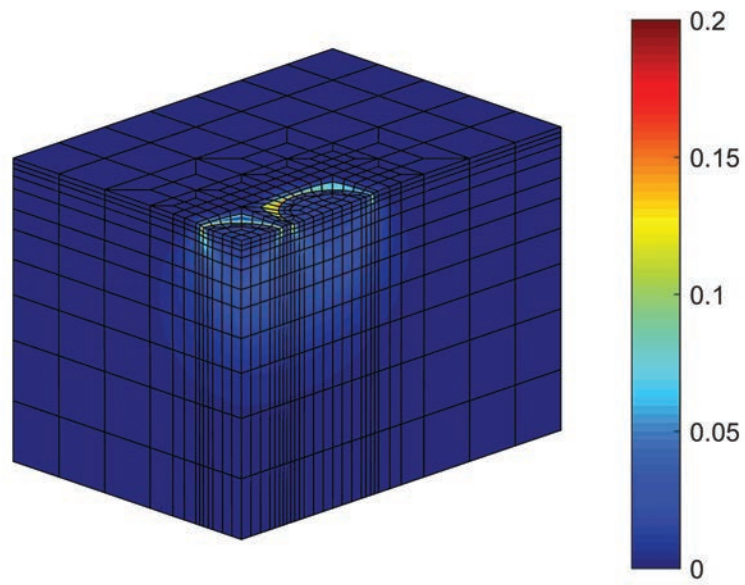


(a)

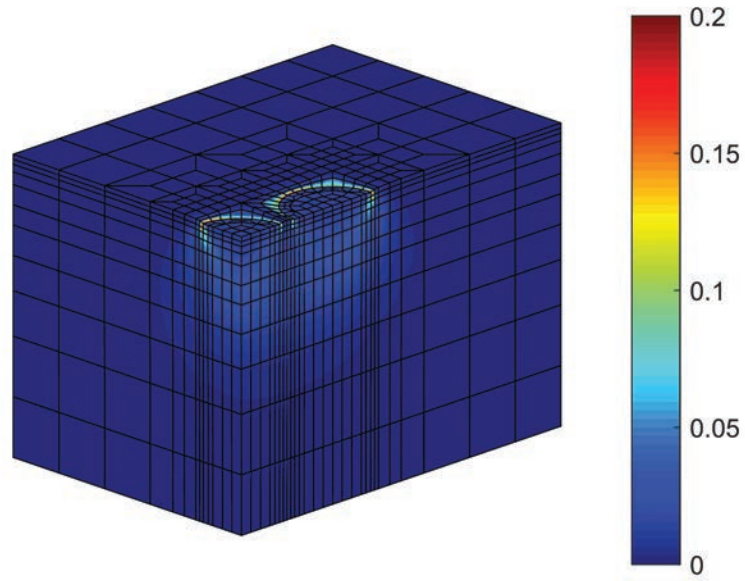


(b)

Fig. 19

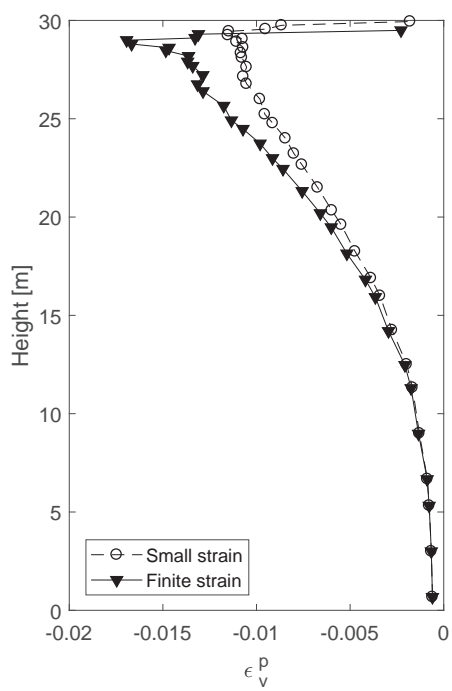


(a)

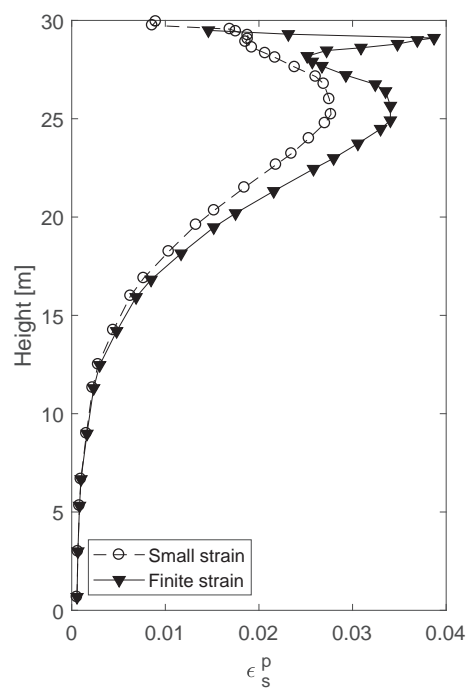


(b)

Fig. 20



(a)



(b)

Fig. 21

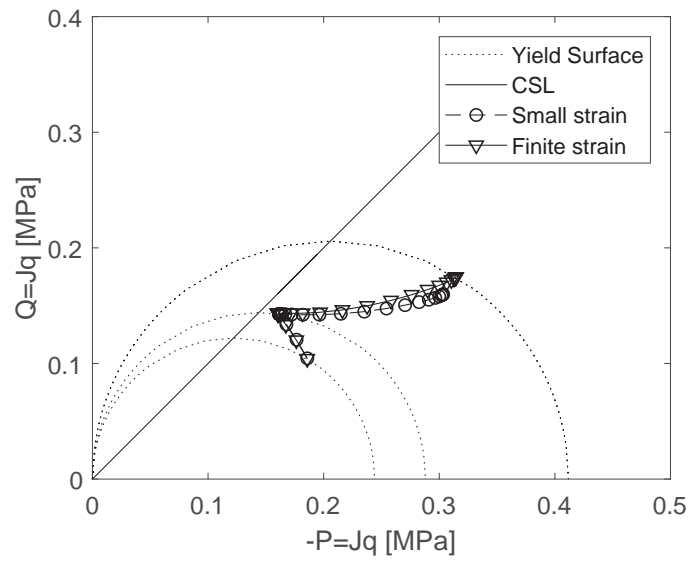
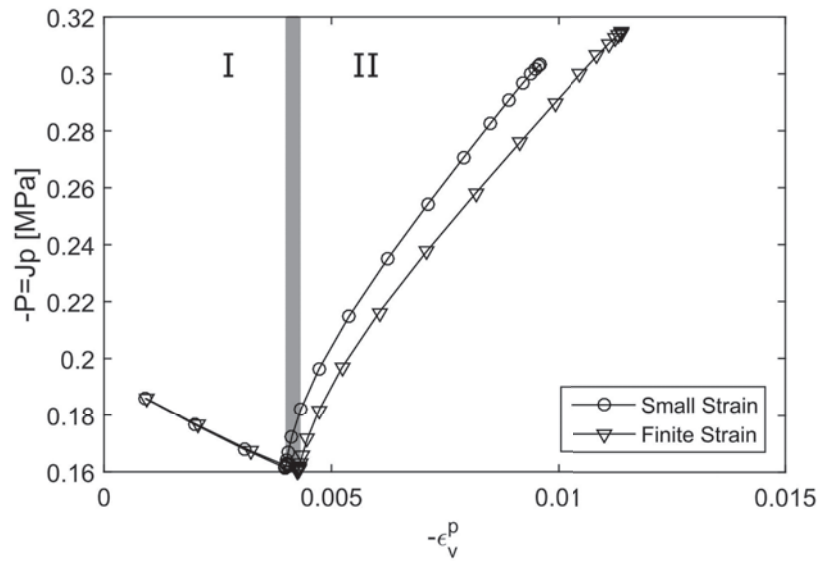
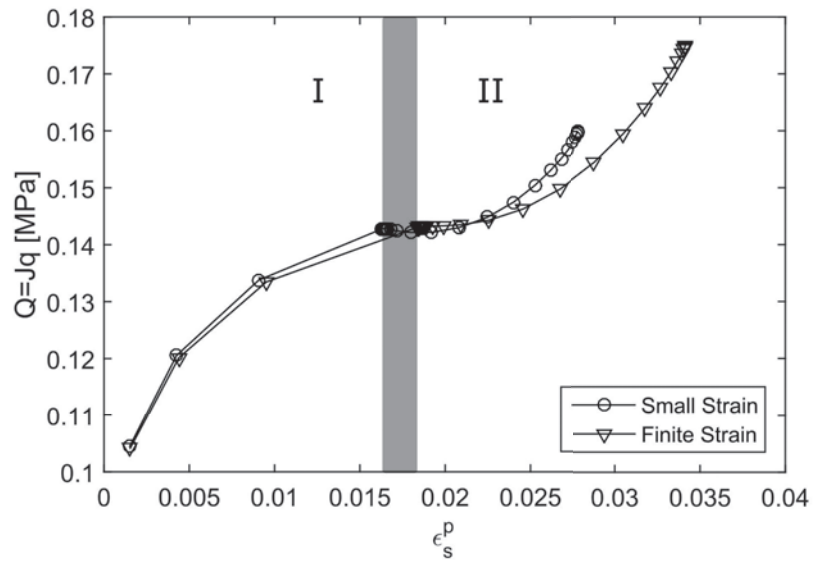


Fig. 22



(a)



(b)

Fig. 23